AGU PUBLICATIONS

JGR

Journal of Geophysical Research: Space Physics

RESEARCH ARTICLE

10.1002/2015JA021823

Key Points:
- Observations of HF-driven plasma turbulence and descending layers are summarized
- Concept of an ionizing wavefront due to accelerated electrons is consistent with the observations
- At high HF powers Langmuir and upper hybrid processes coexist

Correspondence to:
E. Mishin,
Evgeny.Mishin@us.af.mil

Citation:
Mishin, E., B. Watkins, N. Lehtinen, B. Eliasson, T. Pedersen, and S. Grach (2016), Artificial ionospheric layers driven by high-frequency radiowaves: An assessment, *J. Geophys. Res. Space Physics*, *121*, doi:10.1002/2015JA021823.

Received 18 AUG 2015
Accepted 27 FEB 2015
Accepted article online 3 MAR 2016

Artificial ionospheric layers driven by high-frequency radiowaves: An assessment

Evgeny Mishin[1], Brenton Watkins[2], Nikolai Lehtinen[3], Bengt Eliasson[4], Todd Pedersen[1], and Savely Grach[5]

[1]Space Vehicles Directorate, Air Force Research Laboratory, Kirtland AFB, New Mexico, USA, [2]Physics Department, University of Alaska Fairbanks, Fairbanks, Alaska, USA, [3]Birkeland Centre for Space Science, University of Bergen, Bergen, Norway, [4]Physics Department, Strathclyde University, Glasgow, UK, [5]Department of Radiophysics, Lobachevsky State University of Nizhny Novgorod, Nizhny Novgorod, Russia

Abstract High-power ordinary mode radio waves produce artificial ionization in the *F* region ionosphere at the European Incoherent Scatter (Tromsø, Norway) and High Frequency Active Auroral Research Program (Gakona, Alaska, USA) facilities. We have summarized the features of the excited plasma turbulence and descending layers of freshly ionized ("artificial") plasma. The concept of an ionizing wavefront created by accelerated suprathermal electrons appears to be in accordance with the data. The strong Langmuir turbulence (SLT) regime is revealed by the specific spectral features of incoherent radar backscatter and stimulated electromagnetic emissions. Theory predicts that the SLT acceleration is facilitated in the presence of photoelectrons. This agrees with the intensified artificial plasma production and the greater speeds of descent but weaker incoherent radar backscatter in the sunlit ionosphere. Numerical investigation of propagation of *O*-mode waves and the development of SLT and descending layers have been performed. The greater extent of the SLT region at the magnetic zenith than that at vertical appears to make magnetic zenith injections more efficient for electron acceleration and descending layers. At high powers, anomalous absorption is suppressed, leading to the Langmuir and upper hybrid processes during the whole heater on period. The data suggest that parametric upper hybrid interactions mitigate anomalous absorption at heating frequencies far from electron gyroharmonics and also generate SLT in the upper hybrid layer. The persistence of artificial plasma at the terminal altitude depends on how close the heating frequency is to the local gyroharmonic.

1. Introduction

Coupling of high-power high-frequency (HF) pump electromagnetic waves with the ionosphere is mediated by HF-excited plasma turbulence. Its usual manifestations for HF pump waves of ordinary (*O*) polarization are enhanced plasma and ion lines in the incoherent scatter radar (ISR) spectra [e.g., *Stubbe et al.*, 1992; *Cheung et al.*, 2001], elevated electron temperature T_e [e.g., *Rietveld et al.*, 2003; *Blagoveshchenskaya et al.*, 2005], enhanced radioaurora, i.e., HF radar coherent backscatter off enhanced field-aligned irregularities (FAI) $\delta n_{\|}$ [e.g., *Robinson*, 1989; *Senior et al.*, 2004], secondary or stimulated electromagnetic emissions (SEE) [e.g., *Thidé et al.*, 1982; *Stubbe et al.*, 1984; *Leyser*, 2001] due to coupling of electrostatic HF waves with low-frequency (LF) counterparts and FAI, and enhanced optical emissions (artificial aurora) [e.g., *Bernhardt et al.*, 1989; *Kosch et al.*, 2000, 2004; *Pedersen et al.*, 2003]. Optical emissions with the excitation energies 2–18 eV [e.g., *Gustavsson et al.*, 2002, 2006; *Mutiso et al.*, 2008] indicate accelerated suprathermal electrons [*Carlson et al.*, 1982]. It is also worth noting HF-induced ion upflows and density ducts in the topside ionosphere [e.g., *Rietveld et al.*, 2003; *Milikh et al.*, 2010; *Kosch et al.*, 2010].

Matching the pump frequency f_0 to the plasma frequency $f_{\mathrm{pe}} \approx 9\sqrt{n_e}$ kHz and the upper hybrid (UH) resonance, $f_{\mathrm{uhr}} = \sqrt{f_{\mathrm{pe}}^2 + f_{ce}^2}$ defines the plasma resonance (*O*-mode reflection) point at altitude h_0 and UH resonance at $h_{\mathrm{uh}} \approx h_0 - l_n \frac{\omega_{ce}^2}{\omega_0^2}$, respectively [e.g., *Gurevich*, 2007]. Here n_e is the plasma density in cubic centimeters, $f_{ce} = 2.8 \cdot B_0$ MHz is the electron cyclotron (gyro) frequency, B_0 is the geomagnetic field in G, and $l_n = \left|\mathrm{d} \ln n_e / \mathrm{d}h\right|^{-1}$ is the density scale height. The dispersion relation of HF electrostatic waves in weakly magnetized ($\omega_{\mathrm{pe}} \gg \omega_{ce}$) plasma

$$\omega_{\mathbf{k}} \approx \omega_{\mathrm{pe}} \left[1 + (3/2)\, k^2 r_D^2 + \left(\omega_{ce}^2 / 2\omega_{\mathrm{pe}}^2\right) \sin^2 \theta\right] \quad (1)$$

gives Langmuir (L) waves at $\sin^2\theta = k_\perp^2/k^2 \to 0$ and UH waves at $\theta \to \pi/2$. Here r_D is the Debye radius (~1 cm in the *F* region), $\sin^2\theta = k_\perp^2/k^2$, and k is the wave number. Henceforth, "Lo" denotes oblique (or magnetized Langmuir) waves with $0 < \theta < \pi/2$. Another HF branch $\approx\perp \mathbf{B}_0$ is the electron Bernstein (EB) mode, $\omega_{eb}(\mathbf{k})$, with $\partial\omega_{eb}/\partial k_\perp < 0$.

Langmuir waves are parametrically coupled with the *O*-mode pump via low-frequency ($\Omega \ll \omega_0$) density fluctuations (such as ion sound (*S*) waves, $\Omega = \Omega_s \approx kc_s$) or forced, $\Omega^2 < 0$, modulations (ion quasimodes). The former (three-wave) process, $O \to L + S$, is parametric decay (PD_L^O), while the latter is called modulational instability (MI), also known as oscillating two-stream instability (OTSI) [e.g., *Galeev et al.*, 1977; *Fejer*, 1979; *Shapiro and Shevchenko*, 1984; *DuBois et al.*, 1993; *Robinson*, 1997]. Here $c_s = \sqrt{\eta T_e/m_i}$ is the ion sound speed, m_i is the ion mass, and $\eta = 1 + 3T_i/T_e$ at $\omega_{ce} \ll \omega_{pe}$. Note that at $T_e \le 3T_i$, ion sound waves are heavily damped ($\mathrm{Im}\Omega \sim \Omega_s$), so PD_L^O develops in the so-called induced scattering regime. The PD_L^O -excited red-shifted ($\omega_k < \omega_0$) waves are usually described in terms of weak turbulence (WT), while those in the MI regime constitute strong (cavitating) Langmuir turbulence (SLT). Each regime has distinct spectral characteristics, notably the WT "decay lines" and the SLT "caviton continuum" and "free mode" [e.g., *DuBois et al.*, 1993]. Their growth times τ_L are in the order of a few milliseconds. Most important for the artificial plasma production is the SLT acceleration of suprathermal (tail) electrons at energies $\varepsilon \ge \varepsilon_{min} \gg T_e$ (see equation (9)).

UH/EB waves can be excited via decay $PD_{UH/EB}^O$, $O \to \mathrm{UH/EB} + \mathrm{LH}$, and $OTSI_{UH}^O$, $O \to \mathrm{UH} + \delta n_\parallel$ [e.g., *Istomin and Leyser*, 1995; *Kuo*, 2015, and references therein]. Here "LH" designates low-frequency waves near the lower hybrid resonance $\omega_{lhr} \approx \mu^{1/2}\omega_{ce}$, where $\mu = m_e/m_i$ is the mass ratio $\approx 3 \cdot 10^{-5}$ in the *F* region. Another independent source is conversion of the pump wave on FAI, $O + \delta n_\parallel \to \mathrm{UH}$. Trapping UH waves inside striations, i.e., FAI with depleted plasma density $\delta n_{st} < 0$, leads to enhanced ohmic heating in the tenuous regions. As a result, the pressure disbalance forces plasma out. This positive feedback loop leads to the thermal parametric instability (TPI) [e.g., *Vaskov and Gurevich*, 1977; *Grach et al.*, 1981], with the growth time τ_{st} of the order of seconds.

Scattering of an *O*-mode pump off striations into UH waves and slow extraordinary waves, known as the *Z*-mode, leads to (anomalous) absorption of the pump energy *en route* to h_0 [e.g., *Stubbe et al.*, 1994; *Gurevich et al.*, 1996; *Eliasson and Papadopoulos*, 2015], which inhibits PD_L^O and MI in a few seconds. It has become a rule of thumb that Langmuir turbulence plays no role in persistent ($\gg \tau_{st}$) HF-induced phenomena, unless f_0 is in the forbidden band, $|f_0 - sf_{ce}| \le f_{lhr}$, where $OTSI_{UH}^O$, $PD_{UH/EB}^O$, and TPI are inhibited [e.g., *Mjølhus*, 1993; *Stubbe*, 1996].

HF beams pointed vertically propagate along the ionosphere density gradient $\nabla n_0(h)$. This is favorable for the PD_L^O/MI development, as the frequency mismatch

$$\widetilde{\omega}_0(h) = \omega_0/\omega_{pe}(h) - 1 \approx (h_0 - h)/2l_n \tag{2}$$

vanishes at h_0. The same is also true for incidence angles θ_0 within the Spitze cone $\theta_0 < \theta_s = \arcsin\left(\sqrt{\frac{f_{ce}}{f_{ce}+f_0}}\sin\chi\right)$ [e.g., *Mjølhus*, 1990]. Here $\chi \approx 14.5°$ at HAARP and 12°at EISCAT [e.g., *Macmillan et al.*, 2003] is the conjugate of the magnetic dip angle, and in the Northern Hemisphere (downward $\mathbf{B}_o$) the angles θ_0 are positive to the south of vertical. Near $\theta_0 = \theta_s$ and $-\theta_s$, *O*-mode waves are converted to *Z*-mode waves moving upward and downward, respectively [e.g., *Mjølhus*, 1990]. Thus, the regions near to the Spitze angle θ_s and its counterpart $-\theta_s$ are called the upward and downward radio windows, respectively.

For injections outside the Spitze cone, the *O*-mode refraction height $h_r(\theta_0)$ decreases with θ_0, so the frequency mismatch $\widetilde{\omega}_0(h_r)$ increases, seemingly hampering the PD_L^O/MI development. However, low duty cycle (heater on period $< \tau_{st}$) experiments reveal plasma and ion line ISR backscatter with the SLT signatures developing at the magnetic zenith (MZ) in ~10 ms and with greater intensities than those from vertical [*Isham et al.*, 1999; *Oyama and Watkins*, 2007]. Further experiments with extended ($\gg \tau_{st}$) injections also show the dominance of MZ [*Kosch et al.*, 2000; *Pedersen et al.*, 2003; *Rietveld et al.*, 2003]. This is called the *magnetic zenith* effect, although due to the finite width of the HF beam, it is uncertain that the true maximum is along $\mathbf{B}_0$.

At high effective radiated powers, ERPs (P_0 = transmitter output × antenna gain), the regions of enhanced ion line (IL) backscatter from the EISCAT UHF radar, artificial aurora, and SEE descend by 15–20 km from the initial interaction altitude [*Kosch et al.*, 2004; *Dhillon and Robinson*, 2005; *Ashrafi et al.*, 2007; *Borisova et al.*, 2014]. In addition to the HAARP modular UHF incoherent scatter radar (MUIR) and optical imagers, *Pedersen et al.* [2009, 2010, 2011] used the HAARP ionosonde to reveal that descending layers (hereafter, DL) are patches

of newly ionized plasma. *Sergeev et al.* [2013] explored DL using concurrent measurements of SEE, reflected probing signals, and MUIR plasma line (PL) backscatter during frequency-stepping experiments around $4f_{ce}$. The DL-associated optical emissions at ≈732 nm and 427.8 nm (the blue line) indicate electron acceleration above the ionization energies ε_{ion} [*Pedersen et al.*, 2010; *Hysell et al.*, 2014]. These results concern pencil-like radio beams. Conical (or twisted) beam transmissions at MZ with f_0 near $sf_{ce}(h_r)$ ($s = 2-6$) potentially sustain artificial ionization patches for multiple hours (P. Bernhardt et al., Large ionospheric disturbances produced by the HAARP HF Facility, submitted to *Radio Science*, 2016). Henceforth, we focus on the DL during transmissions of usual (pencil) radio beams.

The MZ effect and DL formation have not yet been fully understood. *Gurevich et al.* [2002] argued that self-focusing of the pump beam on striations and associated anomalous absorption define the MZ effect. However, the predicted dependence on f_0 disagrees with the observations. By the same token, in the daytime/twilight experiments [*Pedersen et al.*, 2011; *Sergeev et al.*, 2013] DL started well before striations could develop. In the *Pedersen et al.* [2010, 2011] experiments, DL emerge at $P_0 \geq P_{\text{DL}} \approx 400$ MW for $f_0 < 2f_{ce}$ and $2f_{ce} - f_{\text{uhr}} \leq 5-20$ kHz, when TPI is inhibited [*Mishin et al.*, 2005a]. Thus, the DL formation has been explained in terms of an ionizing wavefront created by the SLT-accelerated electrons [*Mishin and Pedersen*, 2011; *Eliasson et al.*, 2012, 2015]. However, the DL in *Sergeev et al.*'s [2013] experiments were observed only for $f_0 > 4f_{ce}$, consistent with *Gustavsson et al.*'s [2006] observations of stronger 427.8 nm emissions at $f_0 > 4f_{ce}$. These observations suggest that some unknown interplay between Langmuir and UH processes is critical for the creation of artificial ionospheric plasmas.

This paper seeks to extend understanding of this top priority problem through an assessment of the EISCAT and HAARP HF-heating experiments (section 2) and numerical modeling (section 3), as well as expanding on the theory of HF-excited Langmuir turbulence and related effects (Appendix A). Discussion of the observations in terms of the theoretical/modeling results is given in section 4. Overall, we infer the salient DL features: (i1) appearance only for HF beam pointings at MZ in some experiments but (i1*) for all pointings at and between vertical and MZ in the others, (i2) broad IL/PL layers and (i2*) an asymmetry between upshifted and downshifted ion lines, (i3) the SLT persistence along with DL, (i4) appearance for various HF frequencies not limited to the gyroresonance frequencies, (i5) greater speeds at greater HF beam powers, (i6) decreasing speeds after passing the gyroresonance, i.e., at $f_0 < sf_{ce}(h_{\text{gr}})$, (i7) coexistence of UH and Langmuir processes and mitigation of anomalous absorption, (i8) greater descent speeds correspond to weaker PL/IL signals from MUIR, and (i9) more efficient production in the sunlit ionosphere. The listed items will be connected with the pertinent observations in section 2 and discussed in section 4.

2. Observations of Descending Layers

Descending radar echoes and the green line (557.7 nm, the excitation threshold $\varepsilon_{\text{gl}} \approx 4.2$ eV) optical emissions from heating experiments at EISCAT have been observed earlier [*Djuth et al.*, 1994; *Kosch et al.*, 2004; *Dhillon and Robinson*, 2005; *Ashrafi et al.*, 2007], but the first identification of descending layers with artificially produced plasma was in the *Pedersen et al.* [2010] experiments at HAARP.

2.1. Descending Layers of Ion Line Backscatter for $f_0 \sim 5f_{ce}$

Dhillon and Robinson [2005] studied IL backscatter excited by 7.1 MHz ($\geq 5.2f_{ce}(h_r)$) *O*-mode waves at $P_0 = 600$ and 900 MW, with a half-power (−3 dB) beam width $\Delta\theta_b \approx 7°$ and 6°, respectively. The pump beam with the duty cycle 2 min on/2 min off was pointed solely field aligned (into MZ) on 25 September 2002, whereas on 26 September it alternated between vertical (V) and MZ. The EISCAT UHF incoherent scatter radar at $f_r \approx 930$ MHz ($\Delta\theta_b \approx 0.5°$) was observing (Bragg) backscatter at the resonant wavelength $\lambda_r = 2\pi/k_r = c/2f_r \approx 16$ cm from five pointing directions in the magnetic meridian plane with a 5 s time resolution and 1.5 km range gates. These directions are MZ, MZ+6 (≈Spitze), MZ+12 (≈V), MZ-6 (6° south to MZ), and MZ-12 (12° south to MZ). Also, the CUTLASS SuperDARN radar ($f_r = 16-19.5$ MHz) located ≈1000 km south of the heater was observing 14–18 m FAI with a 1 s resolution and 15 km range gates.

Figure 1 is representative of the UHF IL backscatter from V, MZ, and MZ-6 for vertical and MZ injections during 12:34–13:06 UT on 26 September 2002. Overall, there are no effects in MZ-12 and only a few weak returns in MZ+6. For vertical injections, the enhancements in V and MZ are seen only in the first 5 s data dump and thus called *overshoots*. Henceforth, the term "overshoot" designates the transient response of the excited waves over a few seconds and less. For MZ injections, ~20 dB overshoots at MZ turn into descending layers of IL backscatter ≈10 dB less (list items i1 and i4). Hereafter, for brevity, the notation "list items" will be omitted.

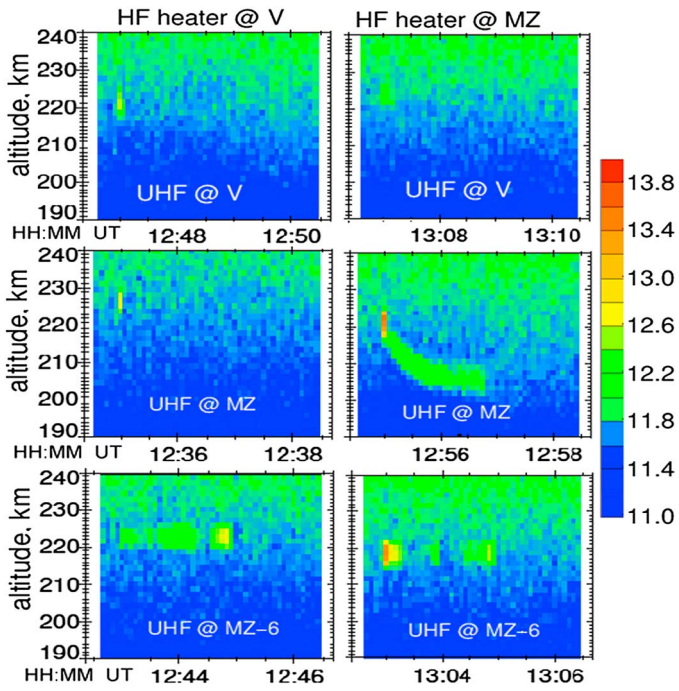

Figure 1. Ion line backscatter amplitudes from the EISCAT UHF radar on 26 September 2002 for (left) vertical and (right) MZ heater pointings. Three rows correspond to three UHF pointing directions: V, MZ, and MZ-6. The altitude versus the time is shown, and the colors give the backscatter amplitudes in log scale. Adapted from *Dhillon and Robinson* [2005].

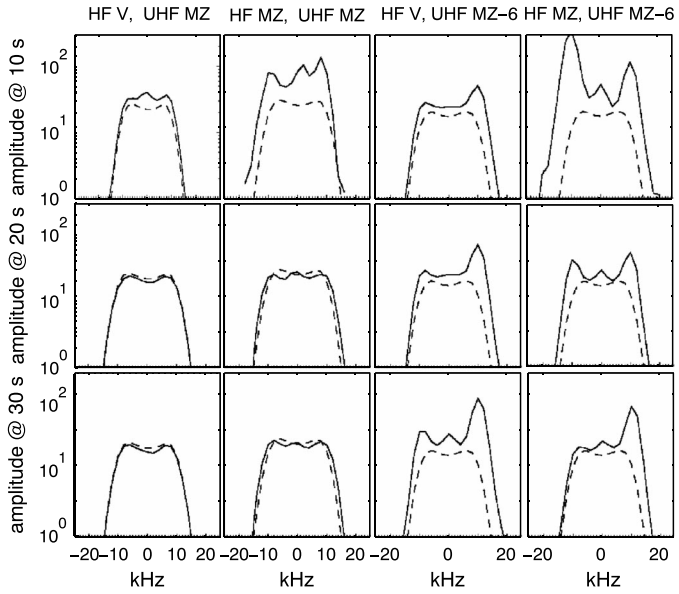

Figure 2. Persistent UHF ion line spectra for UHF radar pointings at MZ and MZ-6 (courtesy of Ranvir Dhillon) for V and MZ HF injections in Figure 1. The dashed (solid) lines correspond to heater off (heater on) periods averaged over two successive 5 s data dumps, i.e., 0–10 s, 10–20 s, and 20–30 s.

The IL backscatter layers start descending from ≈220–225 km at a speed $dh_{re}/dt = v_{re} \approx 250$ m/s and stop in ≈1 min at $h^*_{re} \approx 206$ km. Hereafter, the subscript "re" designates IL or PL radar echoes, while h^*_{xx} means the terminal altitude of a descending feature *xx*. The large altitudinal spread (i2), δh_{re}~10 km, indicates the presence of small-scale irregularities. The IL layers last at the terminus h^*_{re} until the heater is turned off (i3). There appear also persistent layers ($\delta h \sim 5$–7 km) in MZ-6 that do not descend for both vertical and MZ injections. The intensity of the CUTLASS radar coherent backscatter was highest for the area excited by the central part of the heater beam (<2 range gates). Backscatter powers of 10–20 dB at MZ were considerably lower than typically observed 30–50 dB (i7).

Figure 2 exemplifies UHF IL spectra in the directions MZ and MZ-6 for vertical and MZ injections (courtesy of R. Dhillon). The evolving spectra during the heater on period (solid lines) are averaged over two successive 5 s data dumps. After 30 s the spectra remained unchanged until the heater was off. The central spectral peak, one of the SLT features, is readily seen for the entire heater on period for MZ injections (i3) and corresponds to the descending IL feature in Figure 1. The asymmetry between downshifted and upshifted "shoulders" (i2*) indicates different amplitudes of upward and downward propagating ion acoustic waves.

The UHF radar was also monitoring the plasma parameters using long pulses with a 22.5 km range resolution. The background electron temperature near 220 km was typically T_{e0}=0.15 eV. During MZ injections, T_e enhancements at altitudes 180–250 km in MZ were $\Delta T_{mz} \geq 0.17$ eV up to 0.3 eV. Those for MZ-6 were 0.13–0.17 eV and present for the entire heater on interval. The typical values of ΔT_e in MZ-12, MZ+6, and V were ≈0.04–0.08 eV and consistent with pure ohmic heating

[cf. *Gustavsson et al.*, 2010]. For vertical heating, ΔT_e in MZ-12 and MZ+6 were in general lower and not as clear as those for MZ heating, while in MZ-6 the temperature rose to ~0.45 eV.

Note that the actual values of T_e in non-Maxwellian turbulent plasmas can differ from the quoted ones due to the distorted IL spectral shape, particularly at MZ-6. At any rate, non-Maxwellian tails of accelerated electrons (see equation (9)) make virtually no contribution to the mean energy (the temperature). The latter is still defined by the (heated) bulk electron distribution at $\varepsilon < \varepsilon_{\min}$, which remains close to a Maxwellian [e.g., *Mishin et al.*, 2000]. In turn, the location of the spectral peaks is still defined by the ion sound frequency $f_s = \pm k_r c_s/2\pi$ [e.g., *Rosenbluth and Rostoker*, 1962]. Their shift outward from the unperturbed values $f_{s0} = \pm k_r c_{s0}/2\pi$ (Figure 2) clearly indicates plasma heating. As the peak amplitudes are affected by the ion sound turbulence [e.g., *Volokitin and Mishin*, 1995], using the peaks-to-valley ratio to determine the ratio T_e/T_i is precluded. With $T_{e0} = \frac{3}{2}T_{i0}$, calculating $f_s - f_{s0}$ yields $\Delta T_{\mathrm{mz}} \sim 0.2$ eV and $\Delta T_{\mathrm{mz-6}} \sim 0.2-0.4$ eV, consistent with the quoted values.

Contrary to the overshoot behavior at vertical in Figure 1, the *Djuth et al.* [1994] daytime experiments at EISCAT, with $l_n = 40-45$ km for $P_0 \approx 1.1$ GW ($\Delta\theta_b \approx 4°$) and $\theta_0 = 0°-5°$S, show persistent descending IL/PL layers (i1*). In particular, a ≈20 dB, ≈2 s PL overshoot at 6.77 MHz (1 s integration time) was centered near 210 km, with an altitudinal spread of ≈750 m. It was sandwiched between layers ($\delta h \approx 500$ m) of echoes of ~10 dB amplitudes. The overshoot turned into a ~1 km thick layer of ~10 dB echoes (i2). *Djuth et al.* [1994] noted that cloud-like structures in the range-time-intensity plot indicate random small-scale irregularities. After the layer descended by ~3.5 km in 25 s, it has weakened and become more structured while retreating upward by ~1 km in ~30 s. This behavior was routinely observed whenever ≥2 min off periods preceded HF turn on at $P_0 > 500$ MW. The PL/IL spectra, especially the IL central peak, indicate a steady descent of the SLT region (i3). Note that 6.77 MHz was within a few kilohertz of $5f_{ce}$ at 200–210 km. *Djuth et al.* [1994] noted that the PL layers start descending at 25% of full power, with the speed increasing at the 50% and 100% power steps (i5).

2.2. Descending Features for f_0 Around $4f_{ce}$

Figure 3 is representative of the *Ashrafi et al.* [2007] results on 12 November 2001 at EISCAT when the heater transmitted *O*-mode waves at 5.423 MHz and $P_0 = 550$ MW. The F_2 peak plasma frequency (f_oF_2) was ≥ 8 MHz before 17:10 UT, gradually declining to ≈6 MHz at 17:40 UT. The pump beam ($\Delta\theta_b \approx 7°$) was centered at 9°south (S) of vertical and had a 2 min on/off cycle until 16:55 UT. Then, it was scanned in 3° steps between 3°north (N, "-") and 15°S of vertical with a 3 min cycle (2/1 min on/off). Data come from concurrent measurements of the red (630 nm, $\varepsilon_{\mathrm{red}} \approx 2$ eV) and green line emissions at two separate sites, UHF radar ion line backscatter with a 5.4 km range resolution and 5 s integration time and SEE with a 14 s integration time and 300 Hz frequency resolution. The UHF radar ($\Delta\theta_b \approx 0.5°$) was sweeping in 3° steps from 3° to 15°S of vertical in a north-south meridian scan during 15:08–16:55 UT and MZ pointed later on. Black dashes in Figure 3 (bottom) indicate the pump-on periods, and the upper (lower) labels mark the radar (pump) zenith angles.

Shown in Figure 3 (top) are the consecutive SEE spectra with added 10 dB offsets for the heating cycle starting at 16:17 UT. They contain downshifted, $\Delta f = f - f_0 < 0$, and upshifted, $\Delta f > 0$, features. *Ashrafi et al.* [2007] discussed the downshifted maximum (DM) and broad upshifted maximum (BUM) that indicate UH processes [e.g., *Leyser*, 2001]. In particular, the DM and BUM (at $f_0 > sf_{ce}$) are understood in terms of three- and four-wave interactions of UH and LH waves, respectively. We note also the persistent narrow continuum (NC) at $\Delta f > -(5-7)$ kHz, which indicates the SLT development (i3) near the plasma resonance [e.g., *Thidé et al.*, 2005].

As it follows from Figure 3, the BUM peak frequency decreases with time at the rate $r_f \approx 0.2$ kHz/s. *Grach et al.*'s [2008] empirical relation for the BUM peak frequency

$$f_{\mathrm{bum}} = 2f_0 - sf_{ce} + \delta f, \ (\delta f \approx 10 - 15 \text{ kHz}) \tag{3}$$

suggests that $f_{ce}(h_{\mathrm{bum}})$ increases with time, i.e., the BUM generation altitude h_{bum} descends. This spectral feature is hereafter called the BUM_D ("descending"). Using the IGRF model, the descent speed is calculated as $v_{\mathrm{bum}} \approx r_f \left(4df_{ce}/\mathrm{d}h\right)^{-1} \approx 90$ m/s.

Figure 3 (bottom) shows altitude-time plots of raw IL backscatter power for several consecutive HF pump cycles. *Ashrafi et al.* [2007] calculated the matching altitudes h_{gr} ($sf_{ce}(h_{\mathrm{gr}}) = f_0$), h_{uh}, h_0, and h_{bum} using the

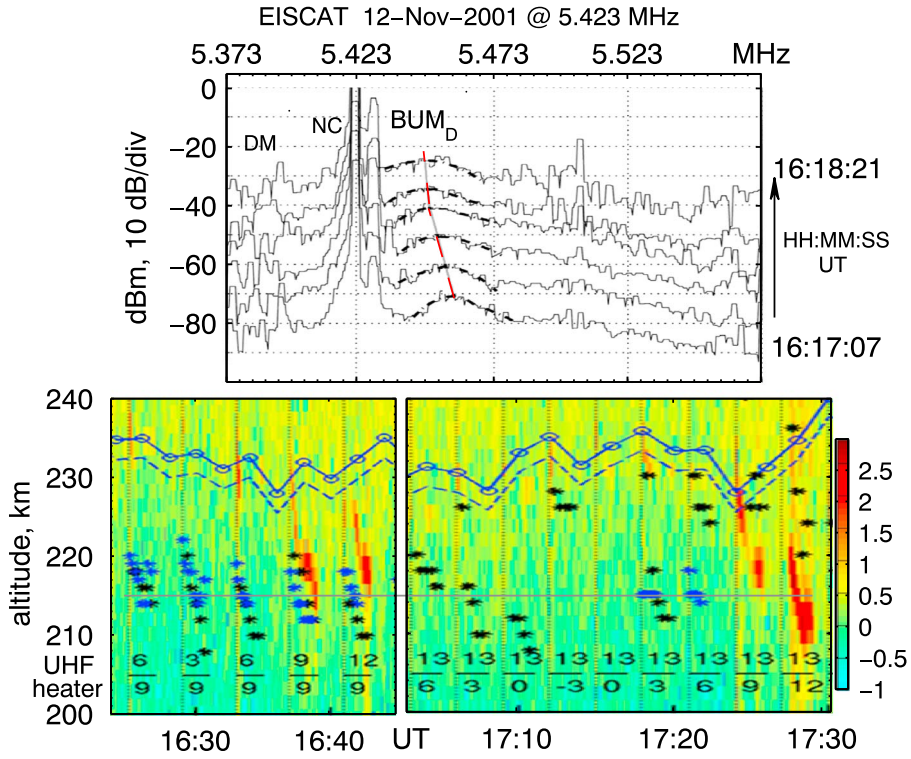

Figure 3. EISCAT experiments on 12 November 2001 at 5.423 MHz. (top) Consecutive SEE spectra from 16:17 to 16:18:21 UT with added 10 dB offsets. The red line indicates the peak BUM$_D$ frequency. (bottom) Raw ion line backscatter power in log scale from the UHF radar during the first (left) and second (right) halves of the experiment with the green line optical height triangulation results (black asterisks) and h_{bum} (blue asterisks) superimposed. The pump-on periods are indicated by black dashes. The upper (lower) labels mark the UHF radar (HF pump) zenith angles. The blue solid (dashed) and dark solid lines indicate h_0 (h_{uh}) and the gyroresonance $h_{gr} \approx 215$ km, respectively. Color codes for the IL raw power in log scale are given at the right. Adapted from *Ashrafi et al.* [2007].

ionosonde data and IGRF model. The heights of the brightest part of the red/green line emissions were triangulated with the average uncertainty of 4–5 km. The green line heights $h_{gl}(t)$ were available only after 16:21 UT. The variation of the nominal heights h_0 and h_{uh} in the background ionosphere is likely caused by a passing atmospheric wave.

Overall, with the pump beam centered at 9°S, enhanced IL echoes in MZ and 9°S radar positions persist during the on period, while only 10–15 s overshoots are seen for 6°and 15°S. The BUM$_D$ feature as in Figure 3 (top) remains throughout. Although Doppler spectra were unavailable, the persistent NC suggests that the enhanced IL echoes come from the descending SLT region (i3 and i7). With the HF beam scanning and the radar pointing in MZ after 16:57 UT, similar overshoots in MZ appear for HF beam zenith angles of −3° to 6°S, as opposed to strong persistent signals for 9° and 12 °S. Clear and consistent BUM$_D$ was seen only near 17:20 UT at 3° and 6°S just above h_{gr}. Descending green line emissions are observed at all injection angles (i1*) except −3°S. On average, layers of persistent IL echoes spread over $\delta h_{re} \sim 3$ km (i2) and descend at a speed $v_{re} \sim 120$–150 m/s until the heater is turned off. The terminal heights h^*_{re} and h^*_{gl} are below h_{gr} for injections in MZ, V, and 3°S (i4); the differences barely exceed the uncertainty range of ~4–5 km though.

We next discuss the *Sergeev et al.* [2013] frequency-stepping experiment on 28 March 2011, 1500–1600 AST (AST = UT-9). The HF beam was pointed at vertical during the first 30 min and at MZ thereafter. Three observational sites were located approximately along the magnetic meridian to the south of the HAARP facility at distances ≈11 (A), 83 (B), and 113 (C) km. Sites A and B were practically under the heating region during injections at vertical and MZ, respectively. The SEE spectra and diagnostic HF radio reflections are very similar at each site, thus indicating broad stimulated radiation and scattering patterns.

O-mode waves were injected at full power ($P_0 \approx 1.8$ GW, $\Delta\theta_b \approx 7°$) and f_0 from 5.73 to 5.88 MHz, stepping by +30 kHz every 5 min; f_oF_2 was ≈6.5 → 6.2 MHz. Each 5 min interval comprises three pumping periods

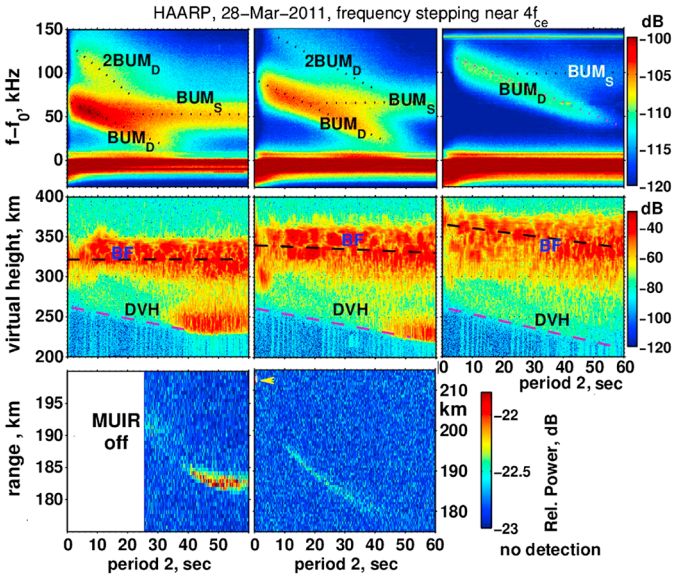

Figure 4. Frequency-stepping experiment at HAARP on 28 March 2011: MZ injections during period 2 at (left column) 5.82, (middle column) 5.85, and (right column) 5.88 MHz. (first to third rows) SEE frequency-time spectrograms over the full range (−50 to 150 kHz), virtual heights of scattered diagnostic pulses, and relative power of MUIR plasma line echoes versus altitude. The arrow shows an overshoot at the onset of period 2. The origin of the time and frequency axes is at the start of period 2 and the pump frequency f_0, respectively. Color codes show the intensities in decibel. Dotted and dashed lines indicate the SEE and virtual height features, respectively (see text). Adapted from *Sergeev et al.* [2013].

followed by 30 s off. Periods 1 and 3 consist of low duty pulses, 20/980 ms on/off, for a total of 30 and 180 s, respectively. A quasi-continuous period 2 comprises 160 ms pulses separated by 40 ms pauses, for a total of 1 min, with the mean $P_0 \approx 1.44$ GW. Diagnostic pulses of 0.1 ms were also transmitted in the middle of each pause with the same power and frequency as the pump. During the last three 5 min steps at f_0 = 5.82, 5.85, and 5.88 MHz, MUIR (f_r = 446 MHz, $\lambda_r \approx$ 33 cm, and $\Delta\theta_b \approx 8.6°$) was measuring magnetic field-aligned PL echoes with 600 m and 10 ms range and time resolution, respectively.

Persistent descending signatures during period 2 appear only for MZ injections (i1) for all frequencies except 5.73 MHz (< $4f_{ce}$). Figure 4 presents the results from site B for f_0 = 5.82–5.88 MHz with the PL measurements from MUIR. SEE frequency-time spectrograms have a frequency (time) resolution of 200 Hz (0.2 s). Figure 4 (top row) displays the full range spectrograms featuring the BUM_S ("stationary"), BUM_D, and $2BUM_D$ centered at f^S_{bum}, $f^D_{bum}(t)$, and $\approx 2f^D_{bum}(t)$, respectively. The BUM_D frequency drifts with time toward f_0 until the frequency offset with f_0 becomes 10–15 kHz (cf., equation (3)) at the terminal time t^*_{bum}. The frequency drift rate r_f is between 1.2 and 1.4 kHz/s for all f_0 and independent on the BUM_D amplitude, while t^*_{bum} increases with f_0 from ≈5 at 5.76 MHz to 40 s at 5.85 MHz and at 5.88 MHz exceed 1 min. The speed of descent, $v_{bum} \approx r_f \left(4df_{ce}/dh\right)^{-1}$, is ≈450–520 m/s. The increase of the overall descent with f_0 is $\Delta h^*_{bum} = v_{bum} \cdot t^*_{bum} \approx 2 \rightarrow 20$ km at f_0 = 5.76 → 5.85 MHz and greater than 30 km at 5.88 MHz. Note that the $2BUM_D$ drifts toward the BUM_S until they "merge."

Virtual (reflection) heights of diagnostic pulses (Figure 4, second row) have the quasi-stationary and descending signatures. The former is due to scattering from the bottomside *F* region (the "BF layer"). As for the low duty periods 1 and 3, the BF layer is initially centered at $h^0_{bf} \approx$ 325, 340, and 360 km at 5.82, 5.85, and 5.88 MHz, respectively. The increase in h^0_{bf} is related to the rise of the *F* layer, consistent with PL overshoots during period 1 at altitudes $h^0_{re} \approx$ 203 km at 5.82 MHz and 213 km at 5.88 MHz [*Sergeev et al.*, 2013, Figure 4]. After about 30 s, the BF layer widens and shifts downward by 20–30 km. Descending virtual height layers are dubbed "DVH layers." They are centered at $h_{dvh}(t)$, appear just after the onset of period 2, and stop at $t^*_{dvh} \approx t^*_{bum}$ + (5–10) s, i.e., well below h^*_{bum}(i4). Near the terminus h^*_{dvh}, the DVH signals at 5.82 and 5.85 MHz intensify until the end of period 2. Their broad scattering pattern and cloud-like structure suggest scattering off randomly distributed small-scale irregularities. This is consistent with the disappearance of the DVH layer and the recovery of the BF to that of period 1 in just a few seconds after the end of period 2 [*Sergeev et al.*, 2013, Figure 3].

Shown next are height-time plots of the PL intensity integrated for 0.5 s. The arrow points to a ~2 s overshoot at 5.85 MHz at the same altitude $h^0_{re} \approx$ 206 km (h_{re} = range·cos(14.5°)) as for 20 ms pulses of period 1 [*Sergeev et al.*, 2013, Figure 4]. The persistent PL signals descend at $v_{re} \approx$ 500–600 m/s. The PL amplitude decreases with f_0, suggesting weaker amplitudes of the detectable 33 cm Langmuir waves, while the descent speed increases (i8). At 5.82 MHz, the enhanced PL signal remains until the end of period 2 at $h^*_{re} \approx$ 175 km, well below $h_{gr} \approx$ 182 km and f_0 outside the forbidden band (i4).

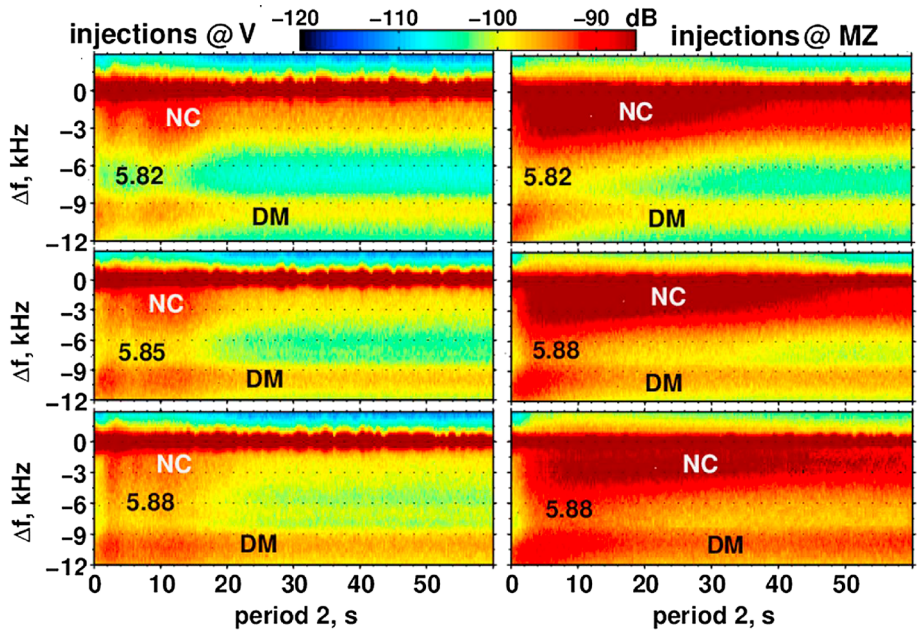

Figure 5. SEE frequency-time spectrograms for vertical and MZ injections during period 2 in Figure 4, zoomed around f_0 = 5.82, 5.85, and 5.88 MHZ. Color codes show the intensities in decibel. The NC and DM features are designated.

Figure 5 shows the bright band around f_0 in Figure 4 zoomed to distinguish the SLT signature (NC) from the UH signature (DM) [cf. *Grach et al.*, 2015, Figure 6]. We note the apparent distinction in the NC and DM behavior at MZ and vertical. The NC spectral width δf_{nc} at vertical contracts in ~15 s so that the NC power ($\propto \delta f_{nc}$) exhibits the overshoot behavior. The NC power at MZ is much stronger. The NC width δf_{nc} gradually approaches to the ~1 kHz band at $\approx t^*_{dvh}$ for 5.82 and 5.85 MHz, while persisting for the entire period 2 for 5.88 MHz (i7). The DM features appear similar at vertical and MZ, thus suggesting the principal role of the NC (SLT) for the descending features in Figure 4 (i3).

Figure 6 presents field-aligned upshifted PL echoes from MUIR during frequency stepping near $4f_{ce}$ on 10 March 2013 at HAARP. The critical frequency f_oF_2 was ≈7.2 MHz indicating steady daytime conditions. *O* waves at frequencies stepping by 20 kHz from 5.74 to 5.88 MHz were injected into MZ at $P_0 \approx 1.8$ GW ($\Delta\theta_b \approx 7°$), with a 2 min cycle (1 min on/off). The PL overshoot heights (arrows) are well above h_{gr} (horizontal lines) at all frequencies except 5.74 MHz. At 5.76–5.88 MHz, persistent signals with an altitudinal spread of ~2–3 km (i2) start after about 0.1–0.2 s at ~(5–10) km below ~1 s overshoots and descend as heating time progresses.

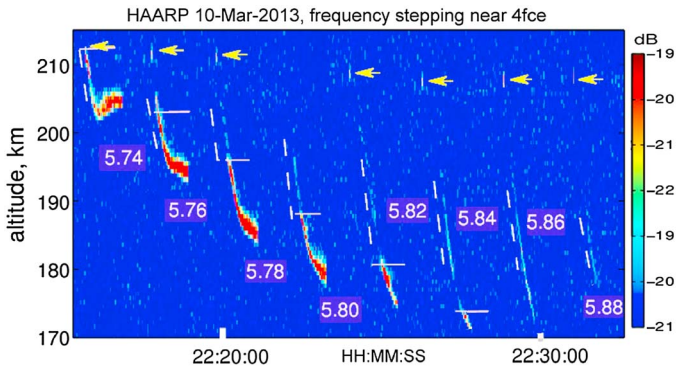

Figure 6. Plasma line backscatter power from MUIR at f_0 stepping by 20 kHz from 5.74 to 5.88 MHz at HAARP, 10 March 2013. Solid horizontal and dashed oblique lines indicate the gyroresonance h_{gr} and the descent rates, respectively. Arrows show initial overshoots. Colors give the backscatter intensity in decibel.

When $h_{re}(t)$ passes through h_{gr}, the radar signals are significantly enhanced, while the descent speed slows down (i6 and i8). Note also that the PL amplitudes at ≥5.84 MHz are quite weak, similar to Figure 4. Concurrent SEE observations (P. Bernhardt, personal communication, 2015) show the BUM_D spectrum similar to Figure 4 (i3 and i7).

2.3. Descending Layers of Ion Line Backscatter for f_0 Around $3f_{ce}$

Figure 7a shows ion line backscatter power from MUIR for 20%, 50%, and 100% of full power $P_0 \approx 1.1$ GW ($\Delta\theta_b \approx 12°$) during 30 s MZ injections at 4.5 MHz ($>3f_{ce}$) on 6 November 2010 at HAARP. Overshoots typically last for

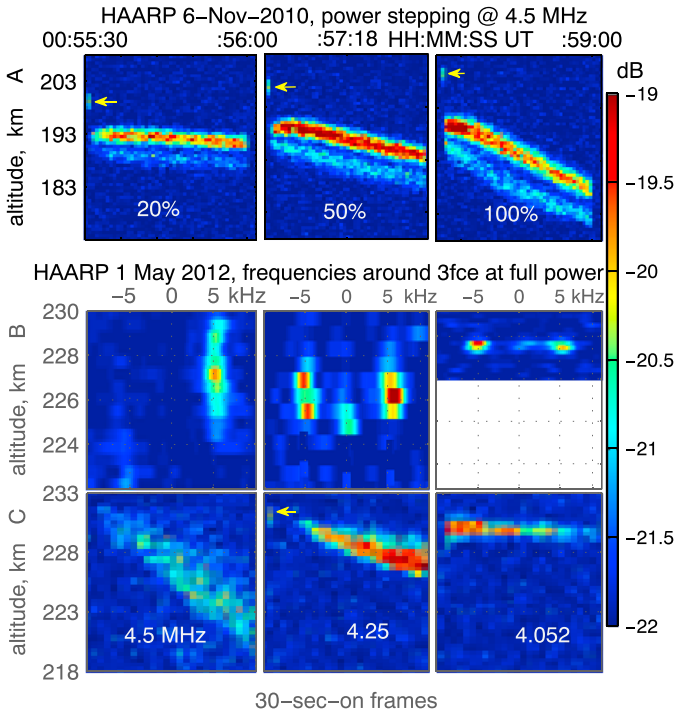

Figure 7. (a) HAARP, 6 November 2010: Ion line backscatter power from MUIR for MZ injections at 4.5 MHz, with ERPs ranging from 20% to 100% of 1.1 GW. (b) HAARP, 1 May 2012: Doppler ion line spectra during the persistent heating phase at full HF power for $f_0 = 4.5$, 4.25, and 4.052 MHz at MZ that correspond to (c) altitude-time plots of raw IL backscatter power. Colors give the backscatter intensity in decibel.

about 0.2 s near h_{mz}, ascending probably due to natural ionospheric variations such as an atmospheric wave and/or small residual density changes from previous HF on cycles. Apparently, at least 220 MW ERP is required to produce persistent descending features during daytime [cf. *Djuth et al.*, 1994]. It is evident that higher HF powers result in more rapid descent ($v_{re} \approx 400$ m/s at 100%) and lower terminal altitudes (i5) Surprisingly, there are two distinct broad (i2) layers of IL echoes closely following each other. The upper layer contains only the positive Doppler-shifted spectral peak (i2*). The weaker, negative Doppler layer is well below the PD_L^O matching height. Note that the IL amplitude in the upper layer at full power is weaker, while the speed is greater than that at 50% (i8).

Shown in Figures 7b and 7c are ion line power spectra observed in MZ on 1 May 2012 for HF frequencies above (4.5 MHz) and below (4.25 and 4.052 MHz), $3f_{ce}$ (i4). Altitude-frequency Doppler spectra in Figure 7b are obtained in the middle of the corresponding altitude-time backscatter power plots in Figure 7c (averaged for 0.5 s). Strong broad signals at positive Doppler and much weaker signals at negative Doppler are seen at different altitudes for 4.5 MHz (i2*). For 4.25 and 4.052 MHz, the usual two decay peaks with Doppler shifts about ±5 kHz at the same altitude and a zero-Doppler central (SLT) peak are seen (i3). Persistent weak signals for 4.5 MHz with an altitudinal spread of ≈ 3 km (i2) descend at a greater speed than stronger signals for 4.25 MHz (i8). Note that the overshoot spectra at 4.5 MHz (not shown) comprise Doppler signals that are "randomly scattered" around zero Doppler (about ±2 kHz), one of the signatures of SLT cavitons, until 30–40 ms. The following 10 ms frames display mainly a "stable" configuration with signals confined to decay ion acoustic frequencies ±4–5 kHz.

2.4. Descending Layers for f_0 Near $2f_{ce}$

Figure 8 exemplifies the DL development during *Pedersen et al.*'s [2010, 2011] experiments at f_0 near $2f_{ce}$, with injections of *O*-mode waves at full power $P_0 \approx 440$ MW ($\Delta\theta_b \approx 18°$). On 17 March 2009, the HF beam at 2.85 MHz was pointed in MZ with a 4 min on/off cycle during 05:05–05:21 UT and then continuously. In addition to 557.7/427.8 nm (green/blue line) systems at the site, a remote (~160 km/N) 557.7 nm imager was looking over HAARP. The 19 November 2009 experiment started with 1 min transmission at $f_0 = 2.85$ MHz then stepped up by 5 kHz, dwelling on each frequency for 36 s to reach 2.95 MHz after 12 min. As a result, the gyroresonance height $h_{gr}(f_0(t))$ (blue stepwise lines) decreased from $h_{gr}^0 \approx 230$ km to $h_{gr}^* \approx 150$ km. The HAARP ionosonde acquired 10 s ionograms every 60 s in March and 10 s in November to determine matching altitudes $h_{uh}(t)$ (green lines), $h_0(t)$ (red), and $h_{2,3}(t)$ for $f_{pe} = 2$ and 3 MHz (black).

The matching heights and $h_{gr}(t)$ on 19 November 2009 are shown for MZ and vertical injections. The MUIR backscatter power from MZ (dark grey) is overlaid. In the overdense ionosphere (frame a), h_0 and h_{uh} are initially below h_{gr} ($2f_{ce} - f_{uhr} \approx 60$ kHz). A ~2 km thick layer of IL echoes (i2) remains just below $h_0 \approx 190$ km until $2f_{ce}(t)$ approaches f_{uhr} + (10–15) kHz and the broad IL layer starts descending. During descent, the IL backscatter layer always remains above $h_{uh}(t)$ with $2f_{ce}(t) - f_{uhr}(t) \approx$ (10–15) kHz. Near the terminus $h_0^* \approx 140$ km, the IL echoes intensify and last until the transmitter turns off. The same pattern is observed on

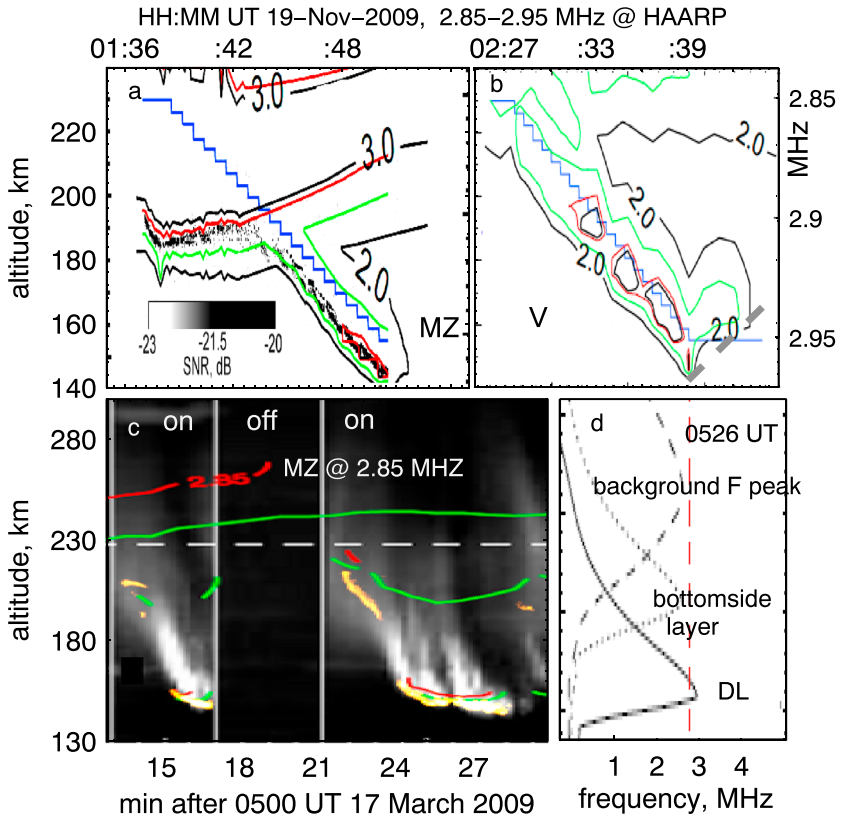

Figure 8. HAARP experiments near $2f_{ce}$ on 19 November (top) and 17 March 2009 (bottom): True height profiles for HF pointing at (a) MZ and (b) vertical, with the gyroresonance $h_{gr}(t)$ (in blue), the terminator height (the thick dashed line), and the MUIR ion line backscatter power from MZ (dark grey) overlaid; (c) altitude-time plot of 557.7 nm emissions from a remote imager during MZ injections with the MUIR ion line backscatter power (in yellow) superimposed (the white dashed line indicates h_{gr}); and (d) true height profiles inverted from the 05:26 UT ionogram. Adapted from *Pedersen et al.* [2010, 2011] and *Mishin and Pedersen* [2011].

14 November, when the background ionosphere became underdense ($f_oF_2 < f_0$) after ≈ 5 min in the heating. However, the plasma frequency within the DL ($f_{pe}^{(DL)}$) reaches f_0. The layer near $h_0^* \approx 150$ km with $f_{uhr}^* \approx 2f_{ce}^*$ persists for 2 min and decays after the solar terminator crossing, i.e., after the sunlit-to-dark transition and absence of photoionization of neutral gas near the terminus (i9).

For the initially underdense ionosphere (frame b), f_{uhr} is already close to $2f_{ce}$ at the very beginning. Although f_oF_2 declines from 2.70 to 2.55 MHz between 02:25 and 02:45 UT, the contours start descending almost immediately. The DL becomes overdense ($f_{pe}^{(DL)} > f_0$) much of the time after 02:32 UT, with $f_{uhr}(t) \approx 2f_{ce}(t) - 15$ kHz on average. Unlike HF pointing in MZ, MUIR does not detect any IL echoes within the first 5 min until 02:32 UT. The signals are very weak from all pointing directions (no vertical beam was used) and nonexistent in MZ. The strongest radar signal from 3°S appears when $f_{pe}^{(DL)}$ reaches f_0. The layer retreats in altitude and disappears following the terminator crossing (i9).

On March 17, strong emissions during 05:13–05:17 UT appear as a diffuse glow and in ~1 min gather into a slowly descending spot-within-ring bull's-eye. The green and blue line emissions at the site develop in concert. This indicates enhanced ionization by ≥18.75 eV electrons during descent. Ionograms also show a secondary bottomside layer gradually descending at ~200 m/s, with h_{uh}^* approaching 200 km. As the central spot descends below h_{gr} to ≈180 km, it turns into a collection of bright field-aligned filaments (a few kilometers in diameter and 10–20 km along $\mathbf{B}_0$) with intensity increased by a factor of 6. The average speed of descent also increases to $v_{gl} \approx 300$ m/s. At ≈160 km the descent slows and ends at $h_{gl}^* \approx 150$ km, with the DL plasma frequency above f_0. Here field-aligned IL echoes, invisible during the fast descent, intensify between h_0^* and h_{uh}^* (i8).

Near h^*_{gl}, the central bright emissions are quenched, whereas an empty ring near 200 km (the bottomside layer) remains in place. The same pattern is realized during a continuous on period beginning at 05:21 UT in the underdense ionosphere. The emissions at h^*_{gl} are quenched themselves several times, initiating the process over again from higher altitudes until the UH resonance ceases. We note that the HAARP experiments with MZ injections at 4.1 and 4.2 MHz ($<3f_{ce}$) on 2 September 2011 (not shown) also show this pattern. Namely, after ≈20–25 s of heating the descending PL echoes at ~215 km almost double its speed up to ≈350 m/s and stop near h^*_{re} ~195 km. Then, the layer is quenched a few times and initiated over again until the end of the transmission.

Overall, the $2f_{ce}$ experiments show that the IL backscatter is persistent for $f_0 < 2f_{ce}$ and intensifies at $2f_{ce} - f_{uhr} \approx$ 5–20 kHz, when the DL formation is also facilitated. Unfortunately, neither spectral IL data nor coherent radar backscatter data were available at that time to specify the LT regime and FAI at high powers. Some important clues can be deduced from low-power (P_0 ≈10 MW, $\Delta\theta_b$ ≈32°) HAARP experiments exploring a frequency pass through $2f_{ce}$ in a decaying ionosphere [*Djuth et al.*, 2005; *Kosch et al.*, 2005, 2007a].

On 4 February 2005, the pump beam at 2.85 MHz was pointed in MZ with a 1 min on/off cycle during 03:00–04:45 UT [*Kosch et al.*, 2007a, Figure 1]. Emissions at 630.0 and 557.7 nm increase near the gyroresonance $h_0 \approx h_{gr}$ [cf. *Mishin et al.*, 2005a], but little change is seen after the double resonance crossing at ≈03:45 UT. However, the Kodiak SuperDARN radar backscatter enhancements at $\lambda_r \approx 19$ m increased from 10–15 dB to 20–25 dB after the crossing. In fact, this transition starts when h_{uh} exceeds h_{gr} by ≈5 km and $f_0 - 2f_{ce}(h_{uh}) > \approx$ 6 kHz, i.e., out of the forbidden band. The crossing particularly affected field-aligned PL backscatter measured by MUIR with range and time resolution of 1.5 km and 10 ms, respectively. Namely, persistent backscatter before the crossing changed to ≤ 2 s overshoots thereafter. Broad SLT peaks with the purely growing mode at f_0 and the WT decay and first cascade lines in persistent PL spectra [*Oyama et al.*, 2006, Figure 3] indicate the coexistence of the WT and SLT regimes (see Appendix A).

On 20 March 2004, the pump beam was pointed in MZ with 4 min (2/2 min on/off) and 10 min (8/2 min on/off) cycles during 06:00–07:00 UT when $f_0 = 2.75$ MHz was less than $2f_{ce}$ [*Djuth et al.*, 2005, Figure 1]. Enhanced 630.0, 557.7, and 777.4 nm emissions indicate accelerated electrons at $\varepsilon \geq 10.7$ eV. *Djuth et al.* [2005] noted only the DM and 2DM SEE spectral peaks. However, the narrow continuum at $\Delta f > -(3-5)$ kHz, alike that in Figure 3, is also clearly seen in their Figure 4. Quite similar NC features have been revealed in the SEE data taken during the March 2011 experiment exploring DL near $2f_{ce}$ at HAARP (M. Kosch, personal communication, 2016).

Recent high-power $2f_{ce}$ heating experiments at HAARP show that the DL formation is typically observed with a broad SEE peak downshifted from the pump by ≈ 0.3–0.5 kHz [*Bernhardt et al.*, 2013]. *Samimi et al.* [2013] have shown that for $f_0 < 2f_{ce}$ and $T_e \geq 3T_i$ the ion acoustic parametric decay (IAPD) instability, UH/EB → UH′/EB′ + IA [*Huang and Kuo*, 1995], develops in the UH layer with a broad growth rate centered at $f_0 -$ (0.3–0.5) kHz and thus termed the peak the IAPD structure or simply IAPD. It has a number of similarities with the so-called downshifted peak revealed and thoroughly explored at EISCAT for $f_0/f_{ce} \geq 3$ [*Leyser*, 2001]. *Mahmoudian et al.* [2013] observed such peak during high-power $3f_{ce}$ heating at HAARP.

In summary, descending layers appear at various frequencies and injection angles but in some experiments only at MZ (i1,i1*, and i4). Greater HF powers correspond to greater DL speeds but weaker MUIR signals (i5 and i8). The descent slows down after passing the gyroresonance altitude h_{gr}, but MUIR signals increase (i6 and i8). The field-aligned IL/PL backscatter persists in, and out of, the forbidden band, $|f_0 - sf_{ce}| \leq f_{lhr}$, around the gyroresonance (i7). In addition to standard SLT/WT features, the IL/PL layers have a notable asymmetry between upshifted and downshifted ion lines and large spread in altitude (i2, i2*, and i3). The DL production is facilitated in the sunlit ionosphere (i9).

3. Modeling of HF-Driven Langmuir Turbulence

Mjølhus et al. [2003] presented a comprehensive review of early works on HF-driven Langmuir turbulence at $P_0 < P_{DL}$, including some results for oblique incidence. *Eliasson et al.* [2012, 2015] performed simulations of Langmuir turbulence and DL in the high-power regime. Before presenting typical nonlinear features at $P_0 > P_{DL}$, we describe (linear) propagation of *O*-mode waves at various incidence angles.

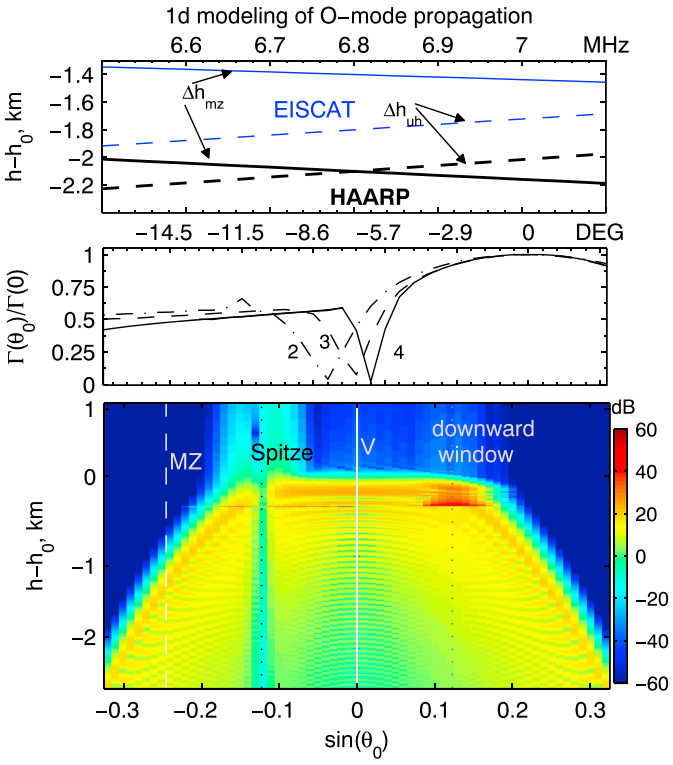

Figure 9. Full wave 1-D modeling of *O*-mode waves for different injection angles and frequencies: (top) $\Delta h_{mz} = h_{mz} - h_0$ (solid lines) and $\Delta h_{uh} = h_{uh} - h_0$ (dashed) at $f_0 = 6.5–7.1$ MHz at EISCAT (thin blue) and HAARP (thick black). (middle) The normalized swelling factor near h_r at HAARP as a function of incidence angle $\Gamma(\theta_0)/\Gamma_0$ at $f_0/f_{ce} = s$ ($s = 2, 3, 4$). (bottom) The altitude-incidence angle distribution of the electric field amplitude normalized to E_{in} at HAARP for 2.85 MHz. MZ, V, and the upward (around the Spitze angle θ_s) and downward (around $-\theta_s$) radio windows are indicated. Color codes for the intensity in decibel are given at the right.

3.1. *O*-Mode Propagation

Assuming the absence of absorption along the path from the ground gives the free space field at an altitude h

$$E_{fs}[\mathrm{V/m}] \approx 5.5\sqrt{P_0[\mathrm{MW}]}/h[\mathrm{km}] \quad (4)$$

Within the Spitze cone, the ratio between the first Airy maximum E_A at $h_A \approx h_0 - l_0$ and E_{fs} gives the swelling factor $\Upsilon_0 = E_A/E_{fs} \approx (2\pi/\sin\chi)^{2/3}(f_0 l_n/c)^{1/6}$. Here $l_0 \approx (c^2 l_n \sin^2\chi/\omega_0^2)^{1/3}$ is the scale length of the Airy function, $\mathrm{Ai}((h-h_0)/l_0)$, and c is the speed of light [e.g., *Mjølhus*, 1990]. For incidence angles $\theta_0 > \theta_s$, as noted by *Mjølhus et al.* [2003], one should consider the caustic rather than the turning point h_r. Nonetheless, $\mathrm{Ai}((h-h_r)/l_\theta)$, with the scale length $l_\theta(\theta_0)$, is still a good representation for the swelling pattern.

To trace an *O*-mode wave up to its turning point, we use *Lehtinen and Inan*'s [2008] full wave algorithm for cold plasma. One-dimensional (1-D) simulations start with the fixed free space field $E_{in} = E_{fs}(h_{in})$ at $h_{in} = 80$ km and the horizontal component of the wave vector $k_x = -\frac{\omega_0}{c}\sin\theta_0 = \mathrm{const}$ (an infinite beam). The x axis is aligned with the magnetic meridian and pointed to the north. The downward geomagnetic field is tilted south at an angle $\chi = 14.5°$ at HAARP and 12° at EISCAT. We do not attempt to model each of the aforesaid experiments rather focusing on general *O*-mode characteristics near the turning point. The magnitude B_0 is assumed constant such that $f_{ce} = 1.425$ MHz. The plasma density profiles at HAARP are taken from the IRI model [*Bilitza et al.*, 2011] on March 2009 at 01:00 AST for $f_0 \le 5.7$ MHz (nighttime). These, for example, give $h_0 \approx 229$ and 279 km and the density scale heights $l_n(h_0) \approx 23$ and 42 km at $f_0 = 2.85$ and 5.7 MHz, respectively. To trace 6.5→7.1 MHz waves, we use Gaussian *F* region altitude profiles with $l_n \approx 45$ km at EISCAT and 50 km at HAARP, giving $h_0(f_0) \approx 280 \rightarrow 289$ km. The electron-neutral collision rate is taken from *Vuthaluru et al.* [2002] (the total electron collision frequency $\nu_e \approx 3 \cdot 10^2\ \mathrm{s}^{-1}$ at ~200 km).

Figure 9 synopsizes the simulation results. Figure 9 (top) shows the height difference $\Delta h_{mz} = h_{mz} - h_0$ and $\Delta h_{uh} = h_{uh} - h_0$ for f_0 stepping by 0.1 MHz from 6.5 to 7.1 MHz at EISCAT and HAARP. As anticipated, the height difference $h_{mz} - h_{uh}$ decreases with f_0. In this particular case, the UH layer is above h_{mz} at $f_0 > 6.8$ MHz ($\approx 4.8 f_{ce}$) at HAARP, while at EISCAT it is still below h_{mz} by ≈0.4 km at 6.8 MHz and 0.2 km at 7.1 MHz. Shown next is the normalized swelling factor $\Upsilon_\theta/\Upsilon_0$ at HAARP for $f_0 = 2.85$ ($2f_{ce}$), 4.275 ($3f_{ce}$), and 5.7 ($4f_{ce}$) MHz as a function of θ_0. It drops at Spitze and approaches the unmagnetized limit $\sin^{2/3}\theta_{mz} \approx 0.39$ [cf. *Mjølhus et al.*, 2003, Figure 12]. As the free space field near the turning point is $E_{fs} \approx E_{in} \cdot h_{in}/h_r$, the "standard" swelling factor $\Upsilon_0 = E_A/E_{fs}$ is equal to $\Upsilon_{in} \cdot h_r/h_{in}$.

Shown in Figure 9 (bottom) is the altitude versus incidence angle log-distribution of the normalized electric field, i.e., $20 \cdot \log_{10}(E/E_{in})$, at HAARP for 2.85 MHz. This plot depicts the salient characteristics of the *O*-mode field near the turning point. The swelling pattern is well approximated by $\Upsilon_\theta(\theta_0)\mathrm{Ai}((h-h_r)/l_\theta)$ for all incidence angles. We note that the scale length l_θ increases with θ_0 so that $l_\theta(\chi) \equiv l_{mz}$ is nearly twice as

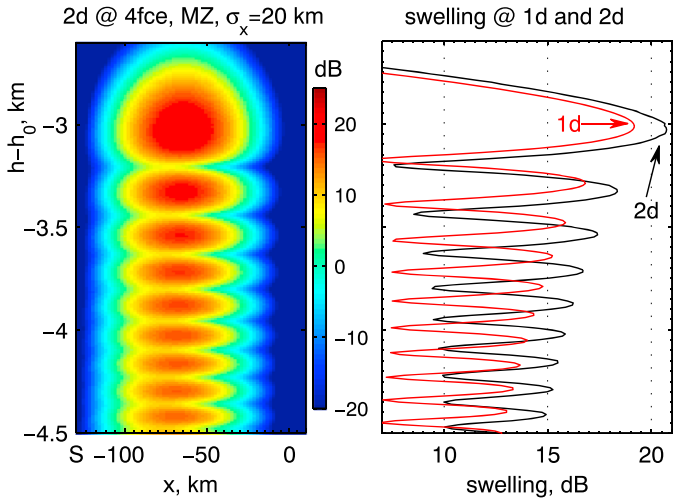

Figure 10. Two-dimensional simulations for $\sigma_x = 20$ km at HAARP. (left) The altitude-meridional distribution of the electric field near h_{mz}. Color codes are for the amplitude normalized to E_{i0} in decibel. (right) The normalized wave amplitude near h_{mz} obtained from 1-D and 2-D simulations.

large as at vertical, l_0. It is worth to note that $|\Delta h_{mz}|$ increases nearly linearly with $l_n(h_0)$ and is about 0.8, 1.3, and 2.7 km at 2.85, 4.275, and 5.7 MHz, respectively. Accordingly, the value of the frequency mismatch at MZ, $\widetilde{\omega}_{mz} \approx -\Delta h_{mz}/2l_n$ (2), is about 0.017. The wave amplitudes in the downward radio window greatly increase just below h_0 due to accumulation of *Z*-mode waves [e.g., *Mjølhus*, 1990]. Waves propagating above h_0 within the upward window were not tracked during this run. However, as expected, quite the same accumulation pattern shifted farther south from the Spitze is present in runs (not shown) that trace reflected *Z* waves.

Two-dimensional calculations for MZ injections have been performed in the Fourier (k_x) domain $k_x \in [k_{mz} \pm \Delta k_x]$ with $k_{mz} = -\frac{\omega_0}{c} \sin\theta_{mz}$. The results in the spatial (x) domain are obtained via inverse Fourier transformation. The initial field profile at $h_{in} = 80$ km is taken as a Gaussian

$$E_{in}(x) = E_y(x, h_{in}) = E_{i0} \exp\left(-(x - x_0)^2/2\sigma_x^2\right) \tag{5}$$

or $E_y(k_x, h_{in}) = C' \exp(-k_x^2\sigma_x^2/2)$ in the k_x domain, where σ_x defines the beam width at h_{in}. For each k_x, the input field components other than E_y are fixed by the condition that for each k_x we have an upward *O*-mode wave. As runs with the k_x interval width Δk_x greater than $4/\sigma_x$ give virtually the same results, it is sufficient to take $\Delta k_x = 4/\sigma_x$. A higher resolution in the x direction is obtained by Fourier interpolation, i.e., extending the k_x interval with zero values. Figure 10 presents the results for 5.75 MHz at HAARP with $\sigma_x = 20$ km corresponding to $\Delta\theta_b \approx 23°$, which depicts the salient 2-D characteristics near h_{mz}. Using $\sigma_x = 10$ km ($\Delta\theta_b \approx 12°$) gives virtually the same results. Left and right frames show the altitude-meridional distribution of the electric field normalized to E_{i0} and the normalized wave amplitude obtained from 1-D and 2-D ($\sigma_x = 20$ km) simulations, respectively. The swelling factor at the beam center exceeds that for 1-D by ≈2 dB.

3.2. One-Dimensional Simulations of SLT and DL

We now present some results of a full wave 1-D modeling of Langmuir turbulence driven by an *O*-mode pump at $f_0 = 3.2$ MHz and various incidence angles θ_0 [*Eliasson et al.*, 2015]. The simulation details are given in [*Eliasson et al.*, 2012; *Eliasson*, 2013]. In brief, the code uses a 1-D geometry, with the computational box from $h = 142$ km to 342 km. A Gaussian F region altitude profile is assumed $n_e(h) = n_m e^{-(h-h_m)^2/l_m^2}$, with $f_{pe}(n_m) = 3.4$ MHz, $l_m = 31.6$ km, and $h_m = 242$ km. The downward magnetic field $B_0 = 0.5$ G ($f_{ce} \approx 1.4$ MHz) is directed at $\chi = 14.5°$S (HAARP) to the vertical. The electron and ion temperatures are taken $T_{e0} = 2T_{i0} = 0.4$ eV, about two times higher than in the quiet ionosphere. The damping rates of Langmuir and ion acoustic waves are set to 10^2 and 10^3 s^{-1}, respectively. Near $h_0 \approx 231$ km, the gradient scale is $l_n \approx 43$ km and the Airy scale $l_0 \approx 75$ m.

Figure 11 exemplifies the evolution of the vertical electric field E_z and ion density fluctuations δn_s near h_r at vertical, 10.5°S, and MZ, with the input amplitude E_{in}=1 and 2 V/m at h_{in}=200 km. Clearly, Airy-like structures of the electric field are set up first. For $E_{in} = 1$ V/m, the first Airy maximum is $E_A \approx 22$ V/m at vertical and ≈13 V/m at MZ [*Eliasson et al.*, 2015, Figure 1]. The nonlinearity parameter

$$w_0 = E_A^2/8\pi n_0 T_e \tag{6}$$

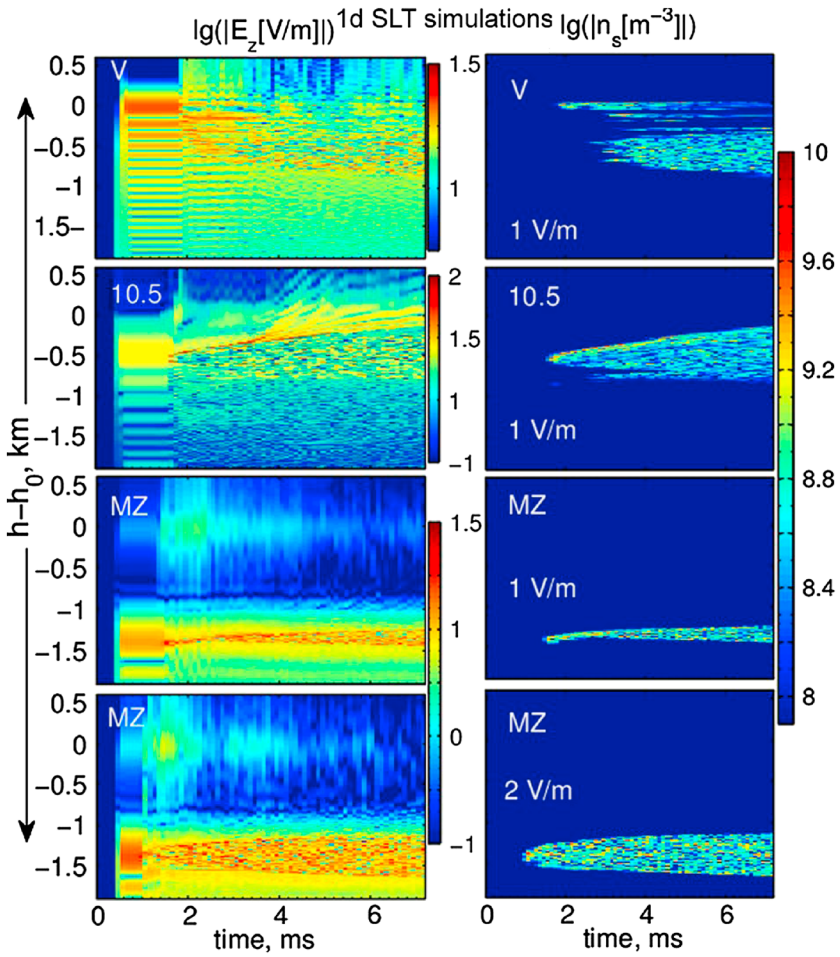

Figure 11. Results of 1-D simulations of SLT at HAARP: Time versus altitude color-coded plots of (left column) $\log_{10}(|E_z[\mathrm{V/m}]|)$ and (right column) $\log_{10}(|\delta n_s[\mathrm{m}^{-3}]|)$ at vertical, 10.5°S, and MZ for the input amplitude $E_{\mathrm{in}} = 1$ and 2 V/m, as indicated in plots. Adapted from *Eliasson et al.* [2015].

is ≈0.26 at vertical and 0.09 at MZ and $\widetilde{\omega}_{\mathrm{mz}} \approx 0.016$ ($\Delta h_{\mathrm{mz}} \approx -1.4$ km). In about 1–1.5 ms this structure within the first few maxima starts breaking into small-scale turbulence. In saturation, solitary wave packets in the SLT region are trapped in density cavitons (Figure 11, right column) of widths $l_a \sim (10-20)\, r_D$ spaced apart by $\sim 50 r_D$. It is seen that the SLT region is sandwiched between the WT regions with turbulent electric fields but without density cavitons. Another notable common feature revealed in full wave modeling is the emergence of *Z*-mode waves around h_0, concurrent with the cavitating turbulence [cf. *Eliasson*, 2008].

The SLT development at vertical (within Spitze $\theta_s \approx 7.7°$) follows a certain pattern. That is, saturation is followed by a gradual downward shift of the turbulent layer. The r.m.s. (root-mean-squared) amplitude δE_{sat} of the saturated turbulent electric fields is smaller than that for the initial stage (the SLT overshoot). The initial stage at 10.5°S and MZ appears the same as at vertical, except for the difference consistent with the frequency mismatch $\widetilde{\omega}_0(h)$ (2). However, at later times the SLT layer at 10.5°S expands in both directions. Ultimately, its upper boundary reaches h_0, while the lower boundary overlaps with the second peak, so the SLT altitudinal extent is $l_{\mathrm{LT}} \sim 5 l_0$. At MZ, the SLT layer remains near the first peak for $E_{\mathrm{in}} = 1$ V/m while for 2 V/m l_{LT} increases with time up to $\sim(3-5) l_0$.

The fast time downward shift and the appearance of *Z*-mode waves can be understood in terms of Brillouin scatter ($O + \delta n_k \rightarrow O'$) and $O + \delta n_k \rightarrow Z$ conversion due to scattering off short-scale cavitons and ion oscillations (e.g., equation (A10)). When SLT develops in lower Airy maxima, the pump energy is scattered en route to h_0,

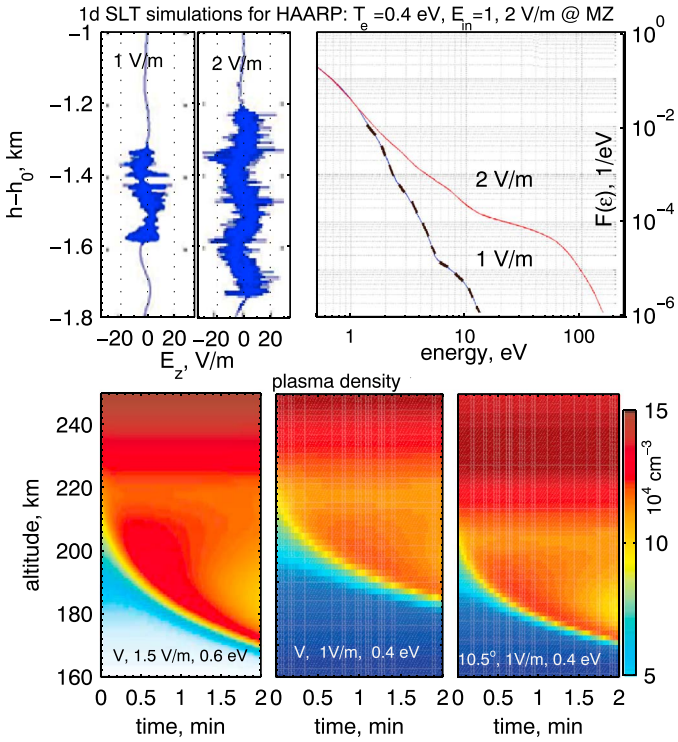

Figure 12. Modeling of the accelerated population and descending layers at HAARP: (top) Turbulent electric fields E_z and the TDF, $F_t(\varepsilon) = F_t(u)\mathrm{d}u/\mathrm{d}\varepsilon$, calculated for MZ injections with $E_{\mathrm{in}} = 1$ and 2 V/m and $T_e = 0.4$ eV. (bottom) Time versus altitude plots of the plasma density in cubic centimeters at V and 10.5°S calculated for various E_{in} and T_e indicated in frames. Adapted from *Eliasson et al.* [2012, 2015].

thereby inhibiting SLT at h_A. Overall, it appears that scattering off cavitons is less harmful for the SLT development at 10.5°S and MZ, where the SLT region gradually expands with time. At 10.5°S, Brillouin scatter seems capable of making *O*-mode waves close to the Spitze cone to produce SLT near h_0.

While crossing an individual caviton of the size $l_a \sim k_a^{-1}$, electrons can gain or lose energy, depending on the phase of the trapped oscillations. Fast electrons, whose passage time is shorter than $\omega_{\mathrm{pe}}^{-1}$, i.e., $v_{\|} = u > \omega_{\mathrm{pe}}/k_a$, experience a localized quasi-stationary field and acquire or lose energy $\sim e|\mathbf{E}|\, l_a$. Here $u = \sqrt{2\varepsilon/m_e}$ is the parallel ($\| \mathbf{B}_0$) velocity. For an isotropic electron distribution, the first-order energy gains are averaged out, thus leaving the net gain $\Delta\varepsilon \propto \left|E_{k_{\|}=\omega_k/u}\right|^2$. Due to a random distribution of cavities in space, electrons will experience a random walk (diffusion) in velocity space and form a non-Maxwellian high-energy tail. This process can be modeled [*Eliasson et al.*, 2012, 2015] by a Fokker-Planck equation for the averaged 1-D (tail) distribution (TDF) $F_t(u)$

$$\frac{\mathrm{d}}{\mathrm{d}t}F_t = \frac{\omega_{\mathrm{pe}}^2}{m_e n_0}\frac{\partial}{\partial u}\frac{W_{\omega_k/u}}{u}\frac{\partial F_t}{\partial u} \equiv \frac{\partial}{\partial u}D(u)\frac{\partial F_t}{\partial u} \tag{7}$$

$$\int W_k \mathrm{d}k = \int_{z_0}^{z_0+l_{\mathrm{LT}}} \mathrm{d}z\, \left|E_z^2\right|/4\pi l_{\mathrm{LT}} \tag{8}$$

Here $d/\mathrm{d}t = \partial/\partial t + u\partial/\partial z$, W_k is the spectral energy normalized by the integral (8), and k is the wave number.

Figure 12 [cf. *Eliasson et al.*, 2012, Figure 8] shows turbulent electric fields E_z and the TDF, $F_t(\varepsilon) = F_t(u)\mathrm{d}u/\mathrm{d}\varepsilon$, calculated for MZ injections at $E_{\mathrm{in}} = 1$ and 2 V/m (cf., Figure 11). Overall, the main part of $F_t(\varepsilon)$ at $\varepsilon_{\mathrm{max}} \geq \varepsilon \geq \varepsilon_{\mathrm{min}}$ can be fitted by a power law ($C_t = \mathrm{const}$)

$$F_t(\varepsilon) \approx C_t \cdot \varepsilon^{-b} \tag{9}$$

The TDF (9) agrees with the prior results [*Galeev et al.*, 1983; *Wang et al.*, 1997], yet b depends on E_{in} and T_e [*Eliasson et al.*, 2012, Table 1]. This is understood as follows. The particle flux into the tail is defined by $D(u_{\mathrm{min}})\left.\frac{\partial F_t}{\partial u}\right|_{u_{\mathrm{min}}}$ in the right-hand side of equation (7). In turn, the tail density $n_t \approx C_t \cdot \varepsilon_{\mathrm{min}}^{1-b}/(b-1)$ is mainly defined by the matching condition, $F_t(u_{\mathrm{min}}) = F_M(u_{\mathrm{min}}, T_e)$ (the ambient Maxwellian distribution). The maximum energy $\varepsilon_{\mathrm{max}}$ depends also on the transit time $\tau_a \sim l_{\mathrm{LT}}/u_{\mathrm{max}}$. Overall, at each incidence angle the simulated spectral width Δk, δE_{sat}, and l_{LT} increase with E_{in}. These factors and the input value of T_e lead to considerable differences in the TDF and DL. In particular, the TDF at 3.5° and 10.5°S is more enhanced than that at vertical due to greater SLT extents l_{LT}. The TDF at MZ for $E_{\mathrm{in}} = 2$ V/m is close to that at vertical for $E_{\mathrm{in}} = 1.5$ V/m [*Eliasson et al.*, 2012, Figure 8, 2015, Figure 10].

The DL development is defined by the input values E_{in}, T_e, and θ_0 [*Eliasson et al.*, 2012, 2015]. Shown in Figure 12 are the DL calculated at vertical and 10.5°S with the TDF for $E_{in} = 1-1.5$ V/m and $T_e = 0.4-0.6$ eV. As discussed in Appendix A, the critical parameter for DL is the density of the ionizing ($\varepsilon > \varepsilon_{ion}$) electrons n_t^{ion}. It follows from the simulations that $\alpha_t^{ion} \equiv n_t^{ion}/n_c$ should exceed $\alpha_t^{dl} \approx (2-6)\cdot 10^{-4}$ for DL to descend from ≈220 km to $h_D^* \approx 180-150$ km [*Eliasson et al.*, 2012, Figure 12]. In particular, $\alpha_t^{dl} \approx 6\cdot 10^{-4}$ is obtained for $T_e = 0.4$ eV and $E_{in} = 1.5$ V/m at vertical [*Eliasson et al.*, 2012, Table 1]. For a Gaussian (2-D) HF beam, a ∼2 dB additional swelling factor at MZ (Figure 10) should reduce E_{in} to $E_{in}^{(2d)} \approx 1$ V/m.

A few remarks are in order (see Appendix A). Although at $w_0 \ll \omega_{ce}^2/\omega_{pe}^2$ the modulational instability is excited in a narrow cone around $\mathbf{B}_0$, $|\theta| \ll 1$, pancake-shaped cavitons (equation (A7)) are not described by the 1-D approximation. In general, either the pumping for the 1-D turbulence or/and T_e should be greater than that for ≥ 2-D in order to achieve the same TDF. Another deficiency is that the TDF is kept unchanged throughout the descent, presuming the same conditions for acceleration. And finally, the presence of photoelectrons significantly enhances the SLT acceleration (see Appendix A), thereby relaxing the dependence on T_e. Therefore, one should exercise caution comparing the 1-D SLT simulations against data.

4. Discussion

The "pure" SLT scenario of the DL formation [*Mishin and Pedersen*, 2011; *Eliasson et al.*, 2012, 2015] implies that in the course of descent the pump wave suffers little absorption en route to h_D. The latter seems contradictory to the concept of anomalous absorption related to the TPI in the UH layer [e.g., *Gurevich et al.*, 1996], especially when the SLT features coincide with DM and BUM_D, i.e., the well-known UH signatures. We first argue that the overall data set shows that strong Langmuir turbulence is the principal cause of the DL formation. Then, the SLT persistence, consequent to mitigation of anomalous absorption, Langmuir processes in the UH layer, and the DL evolution at the terminal altitude are discussed.

4.1. SLT and Descending Layers

For completeness, we outline the SLT features for $P_0 \geq P_{DL}$ or $p_0 = P_0/P_{DL} \geq 1$. For vertical injections at HAARP at $h_0 = 220$ km, $f_0 = 3 \rightarrow 7$ MHz or $10^{-5}n_c \approx 1 \rightarrow 5.4$ cm^{-3}, and $l_n = 40$ km, we get the swelling factor $\Upsilon_0 \approx 28 \rightarrow 32$ and $p_0^{-1/2}E_A \geq 0.5\Upsilon_0 \geq 14 \rightarrow 16$ V/m, thus giving $w_0/p_0 \approx 0.1 \rightarrow 0.03$ for $T_e = 0.3$ eV (see equations (4) and (6)). Taking $p_0(f_0) = 1$ at 3 MHz and 3 at 7 MHz yields $w_0 \approx 0.1$. The swelling coefficient Υ_θ at MZ for a 2-D beam is $\approx 0.8\Upsilon_0$. At any rate, w_0 exceeds the frequency mismatch (equation (2)) $\widetilde{\omega}_A \approx l_0/2l_n \sim 10^{-3}$ and $\widetilde{\omega}_{mz} \approx 0.017$ at vertical and MZ, respectively. Thus, the initial development of plasma turbulence in the first few Airy maxima at MZ and vertical should be nearly the same (cf., Figure 11). As $w_0 \gg w_{sst} \sim 10^{-3}$ (equation (A9)), the turbulence develops in the superstrong (SST) regime and, furthermore, like in isotropic plasmas at $w_0 > \omega_{ce}^2/\omega_0^2$. The latter is easily satisfied for $f_0/f_{ce} \sim 4-5$. Therefore, the SLT acceleration is expected to be more efficient than in the 1-D approximation (Figure 12).

First, we argue that the DL formation is not tied to the BUM_D mechanism, which operates at $h > h_{bum}^* > h_{gr}$ (see equation (3)) and has the minimum excitation threshold $E_{bum} \approx 0.3$ V/m at $f_{bum} \approx f_0 + 3f_{lhr}$ [*Huang and Kuo*, 1994; *Hussein et al.*, 1998]. Note that the free space field E_{fs} (4) exceeds E_{bum} at $h \sim 220$ km for $p_0 > 0.4$, i.e., well below the applied powers. The independence of the DL speed on the BUM_D intensity (Figure 4) and the continuous descent after passing h_{bum}^* (Figures 3–6) show that the BUM_D mechanism is minor for DL. At the same time, the SLT development in the descending region (i3) is indicated by the persistent central IL peak (Figure 2) and NC (Figures 3 and 5). The descent follows the NC power, whereas the DM features appear similar at MZ (with DL) and at vertical (without DL). Furthermore, the descending features and DM follow the onset of heating too rapidly for significant striations to develop, thereby excluding the TPI-related heating. The same is true for the descending PL/IL echoes (Figures 6 and 7). Thus, it appears conclusive to relate DL to the SLT development.

The observation that DL appear in the sunlit ionosphere at $\approx P_{DL}/2$ (see Figure 7a and *Djuth et al.* [1994]) and that the sunlit-to-dark transition quenches the persistent DL at the terminus (Figure 8) indicates more efficient ionization (acceleration) when photoelectrons are present (i9). This is the consequence of the SLT acceleration, which is enhanced in the presence of the ambient suprathermal population (photoelectrons) [e.g., *Mishin et al.*, 2004]. Another consequence is that the DL speed v_D anticorrelates with the MUIR signal amplitude (Figures 4 and 6–8) during daytime (i8). Note that the resonance electron energy for 33 cm waves detected by MUIR is $\varepsilon_r \approx m_e\omega_{pe}^2/2k_r^2 \approx 9$ eV at $f_0 = 6$ MHz and ≈6 eV at 4.5 MHz. Actually, as the wave absorption by the tail electrons increases, collapse can be arrested at greater scales than $1/k_r$, i.e., at $\varepsilon_{min}^{(s)} > \varepsilon_r$. In other words,

while the density of the ionizing ($\varepsilon > \varepsilon_{\rm ion}$) electrons $n_t^{\rm ion}$ and hence v_D (see equation (A13) and *Eliasson et al.*, 2012, Figure 12) increases, the detectable wave energy reduces. At the same time, the persistent NC (Figure 5) reveals the waves with $k < k_r$, undetectable by MUIR. This is consistent with the gap between the initial overshoots and the persistent PL/IL signals (Figures 4, 6, and 7a), which is of the order of the ionization length of accelerated electrons [see *Mishin and Pedersen*, 2011, Figure 2).

The energy flux in the short scales increases due to conversion of long-scale waves on short-scale density oscillations (equation (A10)). The presence of such oscillations is indicated by the large altitudinal spread of the IL/PL layers (i2) and the cloud-like structure of the DVH layers (Figure 4). In the heated plasma ($T_e \sim 0.3-0.4$ eV), short-scale oscillations can be produced by "burned out" cavities in the SLT region [e.g., *Galeev et al.*, 1977] and the heat flux-driven instability (see Appendix A). The latter easily develops at altitudes ~200 km where the mean free path of heated electrons λ_T is ~2–3 km and $l_T = \left|\nabla_\parallel \ln T_e\right|^{-1} \leq 100$ km [cf. *Dhillon and Robinson*, 2005, Figures 5 and 6]. As discussed in Appendix A, this instability leads to the asymmetry (i2*) between downshifted and upshifted shoulders in the IL spectrum (Figure 2).

4.2. Mitigation of Anomalous Absorption and Parametric UH Interactions

Eliasson et al.'s [2015] Figure 11 shows the SLT-driven DL for a broad range of incidence angles, in agreement with some of the data (i1*). Indeed, for $f_0 \sim 2f_{ce}$ (Figure 8), DL appear both at MZ and at vertical. For $f_0 \sim 5f_{ce}$ and $f_0 \sim 4f_{ce}$, the descending (SLT) features have been observed within the Spitze cone [*Djuth et al.*, 1994] and from vertical to MZ (Figure 3), respectively. However, Figures 1 and 2 and Figures 4 and 5 show DL only at MZ (i1) and overshoots at vertical for nearly the same frequencies. We consider anomalous absorption (TPI) as the main factor demarcating the overshoot and persistent behavior.

In particular, anomalous absorption is inhibited in the *Djuth et al.* [1994] experiments, as $f_0 = 6.77$ MHz is within the forbidden band, i.e., $f_0 - 5f_{ce} < f_{\rm lhr}$. Similarly, the TPI development is suppressed for $f_0 \leq 2f_{ce}$ [*Mishin et al.*, 2005a]. Indeed, UH waves exist only for $f_0 > 2f_{ce}$. EB modes in the region $f_{\rm uhr} \leq 2f_{ce}$ at $k_\parallel \to 0$ are not trapped by striations and hence do not contribute to TPI. For small $k_\parallel \ll r_{ce}^{-1}$ (r_{ce} is the thermal electron gyroradius), trapping is limited to waves with relatively small $k_\perp <\approx 5k_\parallel$ [e.g., *Grach*, 1979; *Hysell and Nossa*, 2009]. Such oblique waves are unable to attain short transverse wavelengths; thereby, deep striations necessary for strong absorption are not formed. This conjecture agrees with persistent PL signals at $f_{\rm uhr} \leq 2f_{ce}$, i.e., before the double resonance crossing, and overshoots and increased (by 10–15 dB) Kodiak radar echoes thereafter [*Kosch et al.*, 2007a].

In turn, the DL at MZ and their absence at vertical in Figure 1 can be explained using Figure 9 (top). It gives $h_{\rm mz} - h_{\rm uh} \approx 230$ m ($\approx 3l_{\rm mz}$) at MZ for 7.1 MHz, i.e., the SLT and UH layers overlap. Apparently, scattering of the pump and excited UH waves off short-scale cavitons and ion oscillations (equation (A10)) keeps down the $O \to$ UH coupling and related striations at MZ. However, their development at vertical, where $\Delta h_{\rm uh} \approx 46l_0$ and $\widetilde{\omega}_0(h_{\rm uh}) \gg w_0(h_{\rm uh})$, appears unharmed, in agreement with the increase in the CUTLASS radar backscatter by ~10–20 dB [*Dhillon and Robinson*, 2005].

Such reasoning, however, fails for the DL in Figures 3–7, where $h_{\rm uh}$ is well below $h_{\rm mz}$ and the descent starts and proceeds seemingly regardless of the value of $f_0 - sf_{ce}$ (i4). Thus, we include parametric interactions of the pump-excited (*primary*) UH waves such as IAPD [*Huang and Kuo*, 1995; *Samimi et al.*, 2013], parametric decay $\mathrm{PD}_{Lo}^{\rm UH/Lo}$, i.e., UH/Lo $\to$ Lo′ + LH [*Zhou et al.*, 1994; *Kuo*, 2003], and the $\mathrm{OTSI}_{\rm Lo}^{\rm UH}$, i.e., UH/Lo $\to$ Lo′ + $\delta n_\parallel$ [*Kuo et al.*, 1997]. Such processes rapidly develop at and between vertical and MZ and limit the TPI (striations) development and hence anomalous absorption. This is consistent with the SEE data (Figure 5) showing the UH-LH signature, the DM, rapidly developing and persisting at vertical and MZ (i7).

It is relevant to note that induced scattering of LH waves [e.g., *Galinsky et al.*, 2011] can result in accumulation of the LH energy near $\omega_{\rm lhr}$ and subsequent LH collapse, creating elongated density (LH) cavitons [e.g., *Musher et al.*, 1978; *Shapiro and Shevchenko*, 1984]. *Kosch et al.* [2007a] interpreted the DM [*Djuth et al.*, 2005, Figure 4] and weak backscatter from the Kodiak radar at $f_0 < 2f_{ce}$ by conversion of the parametrically excited UH waves and scattering of the radar beam on LH cavitons, respectively.

The DL development only at MZ (i1) in Figure 4 requires additional arguments. Actually, *Eliasson et al.* [2015] have found that the most favorable incidence angles for DL are 3.5°S and 10.5°S even though the (1-D) swelling factor for 10.5°S is smaller. For real 3-D beams, 3.5°S and vertical are within the half-power beam width, as are 10.5°S and MZ. For a 2-D beam, the swelling factor near MZ increases (Figure 10) to become about the same as at 3.5°S. Thus, the large scale length $l_{\rm LT} \propto l_{\rm mz}$ appears to make HF beam pointings in MZ

more efficient for the SLT development and hence DL. This is consistent with the greater NC power at MZ than that at vertical (Figure 5), alike the aforesaid MZ effect at low powers.

4.3. Langmuir Turbulence in the UH Layer

So far, the SLT development is implied near the turning point h_r, i.e., at and between h_0 and h_{mz}. However, SLT can also develop in the UH layer even at low powers [*Mishin et al.*, 2004]. First, the OTSI$^{UH}_{Lo}$ [*Kuo et al.*, 1997] of the primary UH waves with the r.m.s. amplitude ~0.1 – 0.3 V/m excites oblique short-scale Langmuir waves. These are transferred into long scales via parametric interactions, e.g., induced scattering on ions. The resulting wave condensate is subjected to the modulational instability leading to the SLT regime, albeit weaker than near h_r in the overdense ionosphere (see Appendix A). This mechanism was instrumental in explaining airglow in the underdense ionosphere at MZ at low powers [*Mishin et al.*, 2005b]. As the OTSI$^{UH}_{Lo}$ is facilitated at $f_0 > sf_{ce}$ ($s \geq 3$), the contribution of the SLT acceleration in the UH layer is to be greater above the gyroresonance than below. This helps to explain the emergence of DL [*Sergeev et al.*, 2013], faster descent speeds in Figure 6, and intensification of 427.8 nm emissions [*Gustavsson et al.*, 2006] at $f_0 > 4f_{ce}$.

Similarly, *Samimi et al.*'s [2014] numerical simulations at $f_{uhr} < 2f_{ce}$ and $T_e \geq 3T_i$ show that the IAPD instability in the UH layer is associated with caviton collapse and concomitant electron acceleration along $\mathbf{B}_0$, i.e., in line with the SLT processes. This agrees with the DL development in Figure 8b that starts almost immediately in the underdense ionosphere, where the modulational instability is prohibited until the DL becomes overdense ($f^{(DL)}_{pe} \geq f_0$). Note also that cyclotron acceleration [e.g., *Dimant et al.*, 1992; *Kuo*, 2015, Figure 1] can contribute to the DL formation at small $|2f_{ce} - f_0|$, as with intensified optical emissions at $h_0 \to h_{gr}$ for low powers [*Mishin et al.*, 2005a; *Kosch et al.*, 2007a].

It seems natural to explain the presence of two descending ion line layers at $f_0 = 4.5$ MHz (Figure 7a) by the concurrent excitation of SLT near h_{mz} and h_{uh}. Indeed, the height difference $h_{mz} - h_{uh} \approx 4$ km (at the scale height $l_n = 50$ km) is close to the observed one at 20% and 50% of full power and at the beginning of descent at full power. The weaker signal in the lower layer is consistent with the weaker SLT energy in the UH layer [*Mishin et al.*, 2004]. Let us assume that two temperature profiles, with peaks near h_{mz} and h_{uh}, overlap in such a way that the temperature peak is formed between the layers. Then, the asymmetry in the Doppler-shifted spectra in each layer can be understood in terms of propagation of short-scale, $k > k_r$, ion acoustic waves along $\nabla_{\|} T_e$. Though in this case the heat flux instability is not necessary, it can also contribute to the asymmetry.

4.4. Quenching and Persistence at the Terminus

Mishin and Pedersen [2011] suggested the thermal self-focusing instability near the plasma resonance to be the cause of kilometer-scale bright filaments in the March 2009 experiment, as *Kosch et al.* [2007b] for low powers. According to theory [e.g., *Guzdar et al.*, 1998], kilometer-scale filaments grow initially and in ~10 s break into smaller-scale sizes (tens to hundreds of meters). During descent, the plasma resonance at h_D descends by several kilometers in ~10 s, thereby precluding breaking into small scales. However, in the persistent layer at the terminus h^*_D small-scale irregularities can fully develop for f_0 well under $2f_{ce}(h^*_D)$ and scatter the HF beam, thereby quenching the SLT-related ionization and thus the DL. As soon as the layer decays and irregularities fade out, the artificial plasma can be created again, resembling the quenching and reappearance of the DL in Figure 8c. On the other hand, the instability is suppressed when $f_0 - sf_{ce}$ tends to zero [e.g., *Mjølhus*, 1993; *Starodubtsev et al.*, 2007, Figure 6], in agreement with the DL's persistence at h^*_D in November 2009 (Figures 8a and 8b).

A remark is in order. Even though our main object, the DL, is not related to the persistent IL layers near h_0 at MZ-6 for MZ and vertical injections (Figure 1), this phenomenon is significant enough to be discussed. We suggest that such layers are related to *Z*-mode waves that are efficiently generated by resonant scattering of the pump wave off cavitons in the SLT regions, such as in Figure 11, and also off FAI or LH cavitons near h_{uh} [*Mishin et al.*, 2001]. After reflection on the topside, the *Z*-mode reaches the height of transformation into Langmuir waves slightly below h_0 and farther south to MZ [cf. *Gelinas et al.*, 2003, Figure 12]. As the $Z \to L$ (linear) conversion process is also very efficient, the SLT development in this layer is expected [e.g., *Mishin et al.*, 2001]. The high wave energy, such as around the downward radio window in Figure 9, makes the elevated T_e observed at MZ-6 [*Dhillon and Robinson*, 2005] not surprising. Then, the heat flux instability in the heated plasma provides an explanation of the asymmetric IL spectra at MZ-6 (Figure 2).

5. Conclusion

The salient features of HF-driven plasma turbulence and descending layers of freshly ionized plasma in high-power heating experiments have been summarized. The overall data relate DL to the development of strong Langmuir turbulence, which is revealed by the specific spectral features of incoherent radar backscatter and stimulated electromagnetic emissions. We have performed numerical investigation of (linear) propagation of *O*-mode waves for 1-D and 2-D HF radio beams at various incidence angles, along with the SLT development and DL formation in the 1-D approximation. The swelling factor of a 2-D beam exceeds that of a 1-D beam by about 2 dB, while the characteristic scale length of the swelling pattern at MZ is about twice that at vertical. The greater extent of the SLT region near MZ than that at vertical appears to make HF beam pointings in MZ more efficient for electron acceleration and DL. The presence of the ambient suprathermal (photo)electron population facilitates the SLT acceleration. The consequences of the photoelectrons in the sunlit ionosphere are the decreased DL formation threshold, the greater DL speeds at weaker MUIR signals and stronger NC powers, the gap between the overshoot and persistent PL/IL signals, and the decay of the persistent DL at the terminus after sunlit-to-dark transition.

The data suggest that the SLT persistence near the plasma resonance during descent is the consequence of mitigation of anomalous absorption in the UH layer. In particular, parametric UH interactions mitigate anomalous absorption for heating frequencies outside the forbidden band and also generate Langmuir turbulence in the UH layer. The presence of the second SLT region is consistent with two layers of the MUIR ion line backscatter at $f_0 > 3f_{ce}$, as are the emergence of DL, faster descent speeds, and intensification of 427.8 nm emissions at $f_0 > 4f_{ce}$. The DL persistence at the terminal altitude depends on how close the heating frequency is to the local gyroharmonic. The large altitudinal spread of the IL/PL layers and the cloud-like structure of the DVH layers indicate the presence of short-scale density oscillations. These can be produced in the heated plasma by burned out collapsing cavities and the heat flux-driven instability. The latter leads to the asymmetry between downshifted and upshifted shoulders in the IL spectra and limits the field-aligned heat conductivity.

Overall, the concept of an ionizing wavefront created by accelerated suprathermal electrons agrees with the data. More careful studies, both experimental and numerical, are needed in order to detail the processes involved. Future modeling at various pump frequencies should include parametric interactions in the upper hybrid layer, scattering of the radio beam off cavitons, thermal self-focusing and heat flux instability effects, and the resulting SLT acceleration in the plasma resonance and upper hybrid layers in a self-consistent manner.

Appendix A: Langmuir Turbulence and Related Effects

We present a heuristic description of plasma turbulence driven by pump waves of the amplitude $\mathbf{A}_0$ and frequency $\omega_0 \approx \omega_{pe} \gg \omega_{ce}$ near the plasma resonance h_0. It is based on the Zakharov equations describing slow processes after "filtering out" the fast (HF) variations [e.g., *Zakharov*, 1984]. So the Langmuir field is presented via potentials $\phi = \mathrm{Re}(\Psi(r,t)e^{-i\omega_{pe}t})$ and $\mathbf{E}_l = -\nabla\phi$, with slowly varying ($\frac{d}{dt} \ln|\Psi| \sim \Omega \ll \omega_{pe}$) amplitudes Ψ and $\mathbf{A}_l = -\nabla\Psi$. The pump wave near h_0 is polarized mainly along $\mathbf{B}_0$, i.e., $|\mathbf{E}_\parallel| \gg |\mathbf{E}_\perp|$. Then, the ponderomotive force is almost the same as in isotropic plasma, $\mathbf{F}_p = -\nabla W_\Sigma/2n_e$, accurate to $|\mathbf{E}_\perp^2| / |\mathbf{E}_\parallel^2|$. Here W_Σ is the energy density of the total, pump and electrostatic, HF wavefield. Its quantitative measure is the dimensionless parameter of nonlinearity $w_\Sigma = W_\Sigma/n_0T_e$. Another key parameter is the frequency mismatch $\widetilde{\omega}_0$ (2), since two HF oscillations with frequencies $\omega_0 \approx \omega_1$ exert the ponderomotive force at the beat frequency $\Omega = \omega_0 - \omega_1$.

For $p_0 = P_0/P_{DL} \geq 1$, we get from equation (4) the pump amplitude $A_0 = E_A(\theta_0) = 0.5\Upsilon_\theta\sqrt{p_0}$ at $h_0 = 220$ km. Taking $f_0 = 3$ MHz ($n_c \approx 10^5$ cm^{-3}), $T_{e0} = 0.2$ eV, $l_n = 40$ km, and $\chi = 14°$ gives at vertical $l_0 \approx 75$ m, $E_A \approx 12\sqrt{p_0}$ V/m, and $w_0 = E_A^2/8\pi n_0T_e \approx 0.2p_0$. In the jth Airy peak within the Spitze, the frequency mismatch is $\widetilde{\omega}_{Aj} = \widetilde{\omega}_A \cdot (h_0 - h_j)/l_0$, where $\widetilde{\omega}_A = \widetilde{\omega}_0(h_A) \approx l_0/2l_n \sim 10^{-3}$, while $w_{0j} \approx a_j w_0$ ($a_j \approx 0.36 \to 0.16$ at $h_j/l_0 \approx 10 \to 40$). For $w_0 \gg \widetilde{\omega}_A$, the frequency mismatch can be disregarded, at least in the first few Airy maxima.

With the magnetic correction, the first Zakharov equation becomes [e.g., *Shapiro and Shevchenko*, 1984]

$$\left(i\frac{\partial}{\partial t} + \frac{3}{2}\omega_{pe}r_D^2\Delta\right)\Delta\Psi - \frac{\omega_{ce}^2}{2\omega_{pe}}\Delta_\perp\Psi = \frac{\omega_{pe}}{2}\nabla\left(\delta N_s\mathbf{A}\right) \tag{A1}$$

where Δ is Laplacian and $\mathbf{A} = \mathbf{A}_l + \mathbf{A}_0$. As ions are unmagnetized, the second Zakharov equation for the slow ($\Omega \ll \omega_{pe}$) density variation $\delta N_s = \delta n_i/n_0$ remains

$$\left(\frac{\partial^2}{\partial t^2} - c_s^2\Delta\right)\delta N_s = \frac{1}{16\pi n_0 m_i}\Delta\,|\mathbf{A}|^2 \tag{A2}$$

We disregard collisional and convective damping, assuming $w_0 \gg \max(4\nu_e/\omega_{pe}, 2/kl_n, \mu)$, where k is the excited wave number.

Since $\omega_0/c < k_* = \sqrt{\mu}/3d_e$, the dipole approximation (a uniform oscillating field) can be used even at oblique incidence. At $w_0 \gg \omega_{ce}^2/\omega_{pe}^2$, the magnetic effect can be neglected. In the opposite limit, the modulational instability (MI) develops in a narrow cone $|\theta| \le \frac{\omega_{pe}}{\omega_{ce}}\sqrt{w_0} \ll 1$ around $\mathbf{B}_0$. The MI is inherently tied to the tendency of Langmuir plasmons to accumulate inside density depletions $\delta N_s < 0$ (hereafter, *cavities*). It develops when the excess of the HF pressure inside a cavity exceeds the thermal pressure disbalance $\delta p_e = n_0 T_e \delta N_s$ or

$$w_0 > w_{th} = 3k^2 r_D^2 \tag{A3}$$

As the HF pressure forces plasma out of a cavity, it deepens further and "attracts" yet more plasmons, thereby creating a positive feedback loop. In the supersonic, $w_0 > 3\mu$, regime, the growth rate maximizes at $k_m r_D \approx \mu^{1/6}(w_0/3)^{1/3}$ and then reaches a plateau

$$\Gamma_{mi}(k) \approx \omega_{pe}(\mu w_0/3)^{1/2} \tag{A4}$$

The plateau at $k_m < k \le k_{th} \approx r_D^{-1}\sqrt{w_0/3}$ dominates the phase volume of the pump-excited (primary) Langmuir plasmons.

At $|\delta N_s| > 3k^2 r_D^2$, plasmons are trapped so that intense localized wave packets are formed. Cavities with trapped Langmuir oscillations are termed *Langmuir cavitons* or simply *cavitons*. Their evolution can be described using the following simple arguments [e.g., *Sagdeev*, 1979]. Undamped, undriven ($A_0 = 0$) Zakharov equations conserve the total number of plasmons in cavitons

$$\mathcal{N} \approx \int \mathrm{d}\mathbf{r}\,|\mathbf{E}^2|/8\pi\omega_l = \mathrm{const} \tag{A5}$$

As $|\delta N_s| \ll 1$, the integral (A5) yields $|\mathbf{E}^2| \propto l^{-d}$, where $d = 1, 2, 3$ is the dimension of cavitons of the size l. The wavelengths of the trapped plasmons are also of the order of l, i.e., $k \sim 1/l$. As $k \propto |\delta N_s|^{1/2}$ (trapping), one has $l \propto |\delta N_s|^{-1/2}$, indicating that a deepening cavity narrows (*collapses*) as time progresses. Since $|\delta p_e| \propto |\delta N_s| \propto l^{-2}$ and $|\mathbf{E}^2| \propto l^{-d}$, the thermal pressure will ultimately balance the HF pressure for $D = 1$, thus forming one-dimensional cavitons. In two (three) dimensions, the speed of collapse persists (accelerates) with time.

In the supersonic regime, the right-hand side of equation (A2) is $\Delta\,|\mathbf{E}|^2 \sim l^{-2}\,|\mathbf{E}|^2 \propto |\delta N_s|\,|\mathbf{E}|^2$, while the left-hand side becomes $\partial^2/\partial t^2 \sim (t_\infty - t)^{-2} \sim \tau^{-2}$, with $\tau = t_\infty - t$ and the time of collapse t_∞. These give a self-similar solution $|\mathbf{E}| \propto \tau^{-1}$ and $|\delta N_s| \propto l^{-2} \propto \tau^{-4/d}$. It is valid also in the presence of external pumping, because the trapped plasmons become uncoupled from the pump in the course of collapse. The phase velocities of plasmons in collapsing cavitons decrease as $\sim \omega_{pe} l(t) \propto \tau^{2/d}$. At some "absorption" size, $l \le l_a \sim k_a^{-1} \sim (3-5)r_D$ (< 10 cm), plasmons are absorbed by electrons (the wave energy "burnout") due to Landau and transit time damping. While the HF pressure in the caviton drops and collapse is arrested, a small group of suprathermal electrons gain energy. At $T_e \sim T_i$, an empty cavity $|\delta N_a| \sim k_a^2 r_D^2$ relaxes within $\sim(k_a c_s)^{-1} \sim (3-5)/\omega_{pi} \sim (5-9)10^2/\omega_0$. At $T_e > 4T_i$, short-scale ion sound waves at $\Omega_s \sim k_a c_s$, radiated by burned out cavities, tend to accumulate [*Galeev et al.*, 1977].

The system ultimately reaches a dynamic equilibrium between the long-scale pumping and short-scale transfer by collapsing wave packets into the absorption interval $k > k_a$ [e.g., *Galeev et al.*, 1977]. Here some plasmons are localized in randomly distributed cavitons at different stages of collapse, while others are free. The energy is pumped into cavitons in the long-scale *source* region, $k_L \le r_D^{-1}\sqrt{w_L/3}$, with the energy density W_L comprising the MI-excited long-scale waves. The energy balance equation in the source region is

$$\mathrm{d}W_L/\mathrm{d}t = \nu_{ef} W_0 - \Gamma_{mi}(W_L) W_{cav} \tag{A6}$$

Here W_{cav} is the fraction of the energy in collapsing cavitons, $\nu_{ef} = \alpha_{ef}\omega_{pe}w_L$ is the effective dissipation rate of the pump energy, with a numerical coefficient $\alpha_{ef} \sim 1/3$. Since $\nu_{ef} > \Gamma_{mi}$, the saturated level of turbulent electric fields is smaller than during the initial stage (the SLT overshoot).

Between the source and absorption ($k_a \gg k_L$) regions lies the *inertial interval*, through which the energy is transported by collapsing cavitons. The spectrum in the inertial interval can be found assuming that the spectral energy flow $W_k^{(in)}\mathrm{d}k/\mathrm{d}t$ is preserved. Substituting $k(t) \propto \tau^{-2/d}$ gives a power law spectrum $W_k^{(in)} \propto 1/k^{1+d/2}$ and the total energy of short-scale waves at the absorption boundary $W_a \approx W_{cav}(k_L/k_a)^{d/2}$. In particular, for $W_{cav} \sim W_L$ from equation (A6) one gets $w_L \approx 3\mu^{-1}\alpha_{ef}^2 w_0 \gg w_0$.

Since slow ($\Omega \sim \Gamma_{mi} \ll \omega_{ce}$) electron motion is magnetized, the cavitons at $|\delta N_s| \ll \omega_{ce}^2/\omega_{pe}^2$ are pancake-like, with the dimensions [e.g., *Shapiro and Shevchenko*, 1984]

$$l_\parallel \sim k_\parallel^{-1} \sim r_D\,|\delta N_s|^{-1/2} \sim l_\perp \frac{\omega_{pe}}{\omega_{ce}}\,|\delta N_s|^{1/2} \tag{A7}$$

obtained by balancing the second and third terms in the left-hand side of equation (A1) and using the trapping condition $|\delta N_s| \sim k_\parallel^2 r_D^2 \sim r_D^2 l_\parallel^{-2}$. The variation of the electric field in cavitons in the supersonic regime remains $|\mathbf{E}| \propto \tau^{-1}$, and the self-similar solution is $l_\parallel^2 \propto l_\perp \propto |\delta N_s|^{-1} \propto \tau$. The initial dimensions of pancake-shaped cavitons are defined by equation (A7) with $|\delta N_s| \sim w_L$. Though the number of plasmons in collapsing "pancakes" decreases

$$\mathcal{N} = \int \mathrm{d}\mathbf{r}_\perp \mathrm{d}r_\parallel\,|\mathbf{E}^2|/8\pi\omega_l \propto \sqrt{\tau} \tag{A8}$$

the radiated energy density is greater than $3r_D^2/l_\parallel^2$. So new cavitons of smaller scales emerge and collapse, thereby preserving the total energy flow toward the absorption region, $k_\parallel \geq k_a \gg k_L \sim r_D^{-1}\sqrt{w_L}$. The density variation $|\delta N_s|$ in collapsing cavitons can reach $\omega_{ce}^2/\omega_{pe}^2$ at $l_\parallel^{-1} \ll k_a$. Then, symmetric ($l_\perp \sim l_\parallel$) cavitons with $W_{sym} \sim W_L \frac{\omega_{pe}}{\omega_{ce}}\sqrt{w_L} \ll W_L$ continue to collapse, preserving trapped plasmons until the energy burnout. The corollary to the above is that the 1-D description of SLT is deficient for weakly magnetized plasma, especially at large pump powers. In particular, much greater pumping is required in 1-D to achieve the same short-scale wave energy (the acceleration rate).

The above SLT scenario works for $w_L < 3k_a^2 r_D^2 \sim 10^{-2}$ or $w_0 < w_{sst} \approx 0.1\sqrt{3\mu} \sim 10^{-3}$. Otherwise, MI develops in the whole region from the pump to absorption so that in a steady state collapse plays a minor role and the energy flux through the inertial interval is reduced. In this *superstrong* regime, the energy balance becomes

$$\nu_{ef}W_0 = 2\sum\nolimits_{\mathbf{k}} \Gamma_L(\mathbf{k})W_{\mathbf{k}} \quad \text{at } w_0 > w_{sst} \approx 0.1\sqrt{3\mu} \tag{A9}$$

with $\nu_{ef} \sim \omega_{pe}\mu^{1/3}(w_L/3)^{2/3} > \Gamma_{mi}$ and the Landau damping rate $\Gamma_L(\mathbf{k})$ [*Shapiro and Shevchenko*, 1984]. Another limitation concerns the role of small-scale, $q \gg k_L$, density irregularities, $\delta N_s(\mathbf{r}) = \sum_q \mathrm{Re}(\delta N_q \exp(iqz))$. As a result of conversion, $L_{k_L} + \delta N_s \rightarrow L'_q$, long-scale plasmons are transferred into the short scales. Thereby, the amount of the collapsing energy can be significantly smaller than that without small-scale irregularities.

For wideband random phase irregularities, $|\delta N_q| < 3q^2 r_D^2$, the conversion rate Γ_c is readily derived by averaging equation (A1) over the scale $\sim 2\pi/k_L \gg 2\pi/q$

$$\Gamma_c \approx \sum\nolimits_{\mathbf{q}} \nu_l(\mathbf{q}) \frac{\left\langle |\delta N|^2 \right\rangle_{\mathbf{q}}}{36q^4 r_D^4} \tag{A10}$$

to an accuracy of $\Gamma_c \ll \nu_l(\mathbf{q}) < 3\omega_{pe}q^2 r_D^2$ [e.g., *Mishin and Schlegel*, 1994]. Here $\nu_l(\mathbf{k})$ is the total (collisional + Landau) damping rate and $\left\langle |\delta N|^2 \right\rangle_{\mathbf{q}} = \sum_{\mathbf{q}} \left\langle \delta N_{\mathbf{q}} \delta N_{\mathbf{q}}^* \right\rangle$ is the phase-averaged spectral energy. Applying a similar procedure to the electromagnetic version of equation (A1) [e.g., *Shapiro and Shevchenko*, 1984], with either FAI near h_{uh} [*Mishin et al.*, 2001] or SLT cavitons near h_r [*Eliasson*, 2008] in the right-hand side, one can describe resonant scatter of electromagnetic waves into oblique *Z*- and *O*-mode waves.

At MZ, the swelling coefficient is smaller than Υ_0 by a factor of ≈2 in 1-D and ≈1.25 in 2-D simulations (Figure 10). This does not inhibit the instability even at $p_0 \ll 1$, as long as equation (A3) is satisfied. However, it was so far implied that $w_0 > \widetilde{\omega}_0$. As follows from simulations (e.g., Figure 9), the value of $\widetilde{\omega}_{mz} \approx -\Delta h_{mz}/2l_n$ is of the order of 0.017 ($\gg \widetilde{\omega}_A$). This affects the instability development at smaller w_0. For small mismatches

$\sqrt{\mu\widetilde{\omega}_0} \ll w_0 < \widetilde{\omega}_0$ and $\delta_k \approx \omega_{pe}\left(\frac{3}{2}k^2r_D^2 - \widetilde{\omega}_0\right) > 0$ ($\Omega^2 < 0$), the growth rate reaches maximum $\Gamma_{sm} \approx \omega_{pe}\left(\mu\widetilde{\omega}_0 w_0/8\right)^{1/3}$ at $k_m \approx r_D^{-1}\sqrt{2\widetilde{\omega}_0/3}$. In the MI region at $2\delta_k/\omega_{pe} \le w_0$, with the greatest phase volume, the growth rate is $\Gamma_{mk} \approx \omega_{pe}\mu^{1/2}kd_e \le \Gamma_{mi}$ (equation (A4)). Here the development of turbulence is similar to that for $\widetilde{\omega}_0 = 0$, though the short-scale wave energy is lesser [e.g., *Shapiro and Shevchenko*, 1984].

For $\sqrt{\mu\widetilde{\omega}_0} > w_0$, the pump-driven modulational instability is inhibited, while PD_L^O (or induced scattering at $T_e \sim T_i$) generates red-shifted plasmons at $k \sim k_p \sim r_D^{-1}\sqrt{\widetilde{\omega}_0}$. The waves in the resonance zone of the spectral width $\delta k_* \approx 2\mu^{1/2}/3d_e$ grow at the rate $\Gamma_{ind} \approx \omega_{pe}w_0/8 \gg \nu_e/2$ until at $\tau_{ind} \sim 10/\Gamma_{ind}$ they become unstable. In saturation, their pumping $\Gamma_{ind}(W_0)$ is balanced by their decay $\approx \Gamma_{ind}(W_1)$, with $W_1 = \int_{\delta k_*} d\mathbf{k}W_{\mathbf{k}}$. Therefore, their r.m.s. amplitude $\delta E_1 \equiv A_1$ reaches $\approx A_0$. This process repeats itself in each further step, so the WT cascade spectrum consists of consecutive red-shifted peaks of the amplitudes $\approx A_0$ and widths $\sim \delta k_*$. The wave energy is evenly distributed ($W_k \approx W_0/\delta k_*$) over the WT spectrum with the total energy density $W_{ind} \approx W_0\sqrt{\widetilde{\omega}_0/\mu} \gg W_0$. Ultimately, plasmons converge in the region, $k \le k_c \approx r_D^{-1}w_0/2\mu^{1/2} \ll k_p$, with the energy density $W_c \approx W_0k_c/\delta k_* \approx 3k_c^2r_D^2nT_e$. The plasmon condensate is subject to MI, so the WT and SLT regimes coexist. For $w_0 > \mu$, the supersonic MI (equation (A4)) leads to the energy outflow in collapsing cavities $\sim \Gamma_{mi}(W_c)W_{cav}$. Balancing by the energy influx due to induced scattering, $\approx 2\Gamma_{ind}W_0$, gives $W_{cav} \approx W_0 \ll W_c$.

Whatever their source, the short-scale plasmons are absorbed by a small group of plasma electrons that form a non-Maxwellian high-energy tail $F_t(u)$. It is found from equation (7), with $\partial/\partial z = 0$ and W_k determined from the energy balance in the absorption interval

$$\frac{dW_k}{dt} + \frac{d}{dk}W_k\frac{dk}{dt} = \Gamma_a(k)W_k \tag{A11}$$

where $k(t) \sim \tau^{-2}$ and $\Gamma_a(k)$ is the absorption rate.

A steady state solution of equations (7) and (A11) is a power law function, $F_t(\varepsilon) = C_t \cdot \varepsilon^{-b}$ at $\varepsilon_{max} \ge \varepsilon \ge \varepsilon_{min} \gg T_e$. Numerical modeling of 1-D electron acceleration in a Maxwellian ($F_0 = F_M$) plasma yields $b \approx 1.5$, $\varepsilon_{min}^{(M)}/T_e \approx 10-20$ and the tail density $n_t = \alpha_t n_e \approx 10^{-3-4}n_e$ [*Galeev et al.*, 1983; *Wang et al.*, 1997]. The value of n_t is mainly defined by the matching condition, $F_t(\varepsilon_{min}) = F_0(\varepsilon_{min})$. In the presence of the ambient ("seed") suprathermal population (e.g., photoelectrons), with $F_s(\varepsilon_{min}^{(M)}) \gg F_M(\varepsilon_{min}^{(M)})$, the absorption rate increases so that collapse is arrested at greater scales than in a Maxwellian plasma. As a result, the minimum energy of the tail electrons $\varepsilon_{min}^{(s)}$ greatly exceeds $\varepsilon_{min}^{(M)}$ and n_t significantly increases [*Mishin and Telegin*, 1986]. The obvious corollary is that many more energetic electrons are accelerated during daytime than would be at night [*Mishin et al.*, 2004]. Thus, far, neither numerical SLT simulations include the ambient suprathermal population.

Eliasson et al.'s [2015] simulations show the SLT-driven DL at different incidence angles (see Figure 12). *Mishin and Pedersen* [2011] estimated the DL speed v_D using the fact that accelerated electrons move along the magnetic field to form a stretched "tongue" of newly ionized plasma. Let l_{ion} and τ_{ion} be the $\| \mathbf{B}_0$ extent of the ionization region downward and the time for the plasma at $h_D(t) - l_{ion}$ to reach n_c, respectively. Here n_c is defined by the resonance condition $f_{pe}(n_c) = f_0$. Assuming that the ionization rate $q_{ion} \approx n_t^{ion} \cdot \overline{\nu_{ion}}$ greatly exceeds recombination and diffusion losses gives

$$\tau_{ion} \sim \left(1 - \frac{l_{ion}}{l_n}\right)\left(\alpha_t^{ion}\,\overline{\nu_{ion}}\right)^{-1} \sim 0.8\left(\alpha_t^{ion}\,\overline{\nu_{ion}}\right)^{-1} \tag{A12}$$

Here $n_t^{ion} = \alpha_t^{ion}n_c \approx C_t \cdot \varepsilon_{ion}^{1-b}/(b-1)$ and $\overline{\nu_{ion}} \approx 2\cdot 10^{-8}\left([N_2] + \frac{1}{2}[O]\right)$ s^{-1} is the mean ionization frequency, i.e., $\overline{\nu_{ion}} = \int \nu_{ion}(\varepsilon)F_t(\mathbf{v})d^3v$, at $\varepsilon_{ion} \ll \varepsilon_{max}$. As the ratio $\delta_{il}(\varepsilon) = \nu_{il}/\nu_e$ is small, the accelerated electrons undergo fast isotropization, yielding $l_{ion} \sim v\overline{\delta_{il}^{1/2}/\nu_{ion}}$. Here the frequency of inelastic collisions $\nu_{il}(\varepsilon)$ is $\sim (1-2)\nu_{ion}(\varepsilon)$ at $10^2 > \varepsilon/\varepsilon_{ion} > 1$. At altitudes well below the initial resonance h_0, the ambient density is low, $n_c \gg n_0$, and the speed of descent $v_D \sim l_{ion}\tau_{ion}^{-1}$ becomes

$$v_D \sim \alpha_t^{ion}\overline{\nu_{ion}} \cdot \overline{v\delta_{il}^{1/2}/\nu_{ion}} \sim \alpha_t^{ion} \cdot \overline{v\delta_{il}^{1/2}} \tag{A13}$$

As $\overline{\delta_{il}^{1/2}v} \sim 10^6$ m/s, we get the value of $v_D \sim 10^2$ m/s for $\alpha_t^{ion} \sim 10^{-4}$. Note that v_D contains no direct dependence on the neutral density N_n and hence predicts $v_D \sim$ const, providing that $\alpha_t^{ion} \approx$ const along the path.

Let the ionizing front be initially created at some altitude h_D^0. Then, the seed suprathermal population at lower altitudes will be maintained by degrading earlier accelerated electrons, thereby supporting a self-similar process [*Mishin and Pedersen*, 2011]. As soon as the latter is broken, descent slows down and finally stops even for the same input. Apparently, as the scale length in the front decreases, $l_n^D \sim l_{\rm ion} \sim N_n^{-1}$, the SLT extent $l_{\rm LT}$ and the electron transit time ($\sim l_{\rm LT}/u_{\rm max}$) decrease as $\sim N_n^{-1/3}$, thereby limiting $\varepsilon_{\rm max}$ and thus $n_t^{\rm ion}$. Further, adding inelastic losses $StF_t(\varepsilon) \approx -\nu_{\rm il}(\varepsilon)F_t(\varepsilon)$ in the right-hand side of equation (7) puts additional bounds on $\varepsilon_{\rm max}$ at $h_D < 160$ km [*Mishin and Pedersen*, 2011]. That is, when $\nu_{\rm il}(\varepsilon_{\rm max})$ exceeds the acceleration rate $mD(u_{\rm max})/8\pi\varepsilon_{\rm max}$, the increase of $\varepsilon_{\rm max}$ stops [*Volokitin and Mishin*, 1979]. Another factor is that a stretched ($\| \mathbf{B}_0$) tongue of the DL plasma affects the pump propagation [cf. *Gurevich et al.*, 2002]. Apparently, this effect increases at low altitudes where $n_0(h_D) \ll n_c$ and the *O*-mode index of refraction is mainly defined by the DL plasma.

Thus, far, the plasma temperature is implied unchanged, which holds for time scales much shorter than the electron heating time $\tau_T \sim$0.1–1 s. The perturbed electron temperature, $T_e = T_{e0} + \Delta T_e$, is derived from the heat balance

$$\frac{3}{2}n_0\frac{\partial}{\partial t}\Delta T_e \approx \nu_e W_\Sigma - \nu_e\gamma_{\rm il}\Delta T_e - \nabla_\| \mathbf{q}_T \tag{A14}$$

$$q_T \approx 6n_eT_e\nu_{Te}K_T\,{\rm sign}(-\nabla_\| T_e) \tag{A15}$$

Here $\nu_e W_\Sigma$ is the collisional (ohmic) heating rate, q_T is the electron heat flux, $K_T = \lambda_T\left|\nabla_\| \ln T_e\right| = \lambda_T/l_T$ is the Knudsen number, and $\lambda_T = \nu_{T_e}/\nu_e$. It is implied that $K_T \ll 1$ and $\nu_e \approx \nu_{ei}$. The coefficient of inelastic losses at 220 km, $\gamma_{\rm il}(T_e) \approx (0.3-1)\cdot 10^{-3} - 10^{-2} - 1.5\cdot 10^{-2}$ at $T_e \approx (0.15-0.22) - 0.38-0.43$ eV, is calculated using *Majeed and Strickland* [1997] tabulations. The thermal conduction balances $\nu_e W_\Sigma$ at $K_T = K_c = (w_\Sigma/6)^{1/2}$. At $K_T < K_c$, equation (A14) yields $\Delta T_e = \Delta T_\infty \sim 2W_\Sigma/3n_0\gamma_{\rm il}(T_\infty)$ or $T_\infty \sim$0.35 eV at $T_{e0} = 0.2$ eV and $W_\Sigma/n_0T_{e0} \sim 10^{-2}$. The steady state is achieved at $K_T = K_\infty \sim K_c(T_\infty)$.

If T_∞ exceeds $\sim 4T_i \approx 0.3-0.4$ eV and $K_T > 2\mu^{1/2}$, the heat flux-driven instability can develop in the heated region [e.g., *Forslund*, 1970; *Mishin*, 1974]. For $\lambda_T \geq 1$ km, this condition is satisfied for $l_T \sim 100$ km. Far beyond the threshold, the saturated ion sound spectrum is close to $W_k^s \propto W_s \ln(1/kd_e)\cdot k^{-3}$ at $k_{\rm is} \leq k \leq r_D^{-1}$ (the Kadomtsev-Petviashvili spectrum) [e.g., *Kadomtsev*, 1965]. Here the energy density $W_s \sim 10^{-2-3}n_0T_e$, with the spectral maximum at $k_{\rm is}$ and a lower frequency cutoff at $k_{\rm min} \sim (0.05-0.1)/r_D$ (see details and references in *Mishin and Fiala* [1995]). As far as the k_{is} value is concerned, it varies from $\sim (0.2-0.3)/r_D$ to $\sim 0.6/r_D$ in different experiments and simulations where an energetic ion tail is formed. When the ion tail is absent, the spectrum maximizes just above the low-frequency cutoff and the waves are mainly field aligned.

The ion tail occurs at low ion-neutral collisions such as in the *F* region. In this case, waves at $k < 0.6/r_D$ are highly oblique (angles θ up to $\sim \pi/2$), while those at $k \geq 0.6/r_D$ turn to be more field aligned. While waves propagate along $\nabla_\| T_e$, i.e., downward above, and upward below, the temperature peak, their wave numbers decrease and may become detectable by UHF radars. Apparently, greater values of K_T at higher altitudes favor the instability above the T_e peak and thereby the upshifted shoulder in the excited IL Doppler spectra. Another important outcome of this instability is that the heat flux in turbulent plasma is reduced to $q_{\rm turb} = \kappa_{\rm turb}n_eT_e\nu_{Te}$ with $\kappa_{\rm turb}$ in the range $\approx 7.5\mu^{1/2}$ to $\approx \mu^{1/4}$ [*Mishin*, 1974; *Bychenkov et al.*, 1988], thus severely limiting the heat transport at $K_T \gg 2\mu^{1/2}$.

Notation

$\mathbf{B}_0$	the ambient magnetic field
BF layer	the region of scattering from the bottomside *F* region
BUM	broad upshifted maximum
DM	downshifted maximum
DL	descending layers
DP	the downshifted (SEE) peak
DVH	descending virtual height of reflection
E_A	the first Airy peak amplitude
$E_{\rm bum}$	the threshold amplitude for the BUM generation
$E_{\rm fs}$	the free space field

E_{in}	the input amplitude of the pump wave (section 3)
EB	electron Bernstein waves
FAI	field-aligned irregularities
F_M	the Maxwellian distribution
$F_0 = F_M + F_s$	the total ambient electron distribution
F_s	the distribution of ambient suprathermal electrons (e.g., photoelectrons)
$F_t(u)$	the accelerated tail distribution function (TDF)
C_t	the const in the power law approximation (equation (9))
IAPD	ion acoustic parametric decay UH/EB $\rightarrow$ UH$'$/EB$'$ + IA
IL and PL	ion and plasma lines
Knudsen number	$K_T = \lambda_T \left\vert \nabla_{\parallel} \ln T_e \right\vert = \lambda_T / l_T$
L and UH	Langmuir and upper hybrid waves
LH and S	lower hybrid and ion sound (ion acoustic IA) waves
Lo	oblique (magnetized) Langmuir waves
MI	modulational instability
MUIR	the (HAARP) modular UHF incoherent scatter radar
NC	narrow continuum
OTSI	oscillating two-stream instability
$\text{OTSI}^{\text{uh}}_{\text{Lo}}$	oscillating two-stream instability of the UH pump UH $\rightarrow$ UH $\rightarrow$ Lo + $\delta n_{\parallel}$
PD^{O}_{L}	parametric decay $O \rightarrow L + S$
$\text{PD}^{O}_{\text{uh/eb}}$	parametric decay $O \rightarrow$ UH/EB + LH
$\text{PD}^{\text{uh}/L}_{\text{uh}/L}$	parametric decay UH/Lo $\rightarrow$ UH$'$/Lo$'$ + LH
P_0	effective radiated power (ERP)
$P_{\text{DL}} \approx 400$ MW	the threshold ERP for descending layers at $2f_{ce}$
Primary waves	waves excited by the pump wave
SEE	stimulated electromagnetic emissions
SLT	strong Langmuir turbulence
SST	superstrong (Langmuir) turbulence (equation (A9))
Striations	FAI with depleted plasma density $\delta n_{\text{st}} < 0$
TPI	thermal parametric instability
WT	weak turbulence
W_k	the wave spectral energy density
$f^{(\text{DL})}_{\text{pe}}$	the plasma frequency within the DL
h_o	the reflection (plasma resonance) height at vertical
h_A	the first Airy maximum altitude
h_D	the descending layer altitude
h_{gl}	the altitude of the region of green line emissions
h_{gr}	the gyroresonance matching height, $sf_{ce}(h_{\text{gr}}) = f_0$
h_{mz}	the turning points at the magnetic zenith (MZ)
h_{uh}	the upper hybrid resonance height $\Delta h_{\text{uh}} = h_{\text{uh}} - h_0$ and $\Delta h_{\text{mz}} = h_{\text{mz}} - h_0$
h_{re}	the altitude of the region of IL/PL radar echoes
h^*_D	the DL terminal altitude
h^0_{xx}	the start altitude of the descending feature *xx* (*re*, *bum*,*gl*, etc)
h^*_{xx}	the terminal altitude of the descending feature *xx*
l_0	the scale length of the Airy (swelling) pattern at vertical
l_θ	the scale length of the swelling pattern at oblique incidence
l_{mz}	the scale length of the swelling pattern at MZ
l_{LT}	the altitudinal extent of the SLT region
l_n	the density scale height
l_T	the electron temperature scale height
n_c	the critical plasma density defined by the resonance condition $f_{\text{pe}}(n_c) = f_0$
n^{ion}_t	the density of the ionizing ($\varepsilon > \varepsilon_{\text{ion}}$) electrons $p_0 = P_0/P_{\text{DL}}$
r_D	the Debye radius
v_D	the speed of descent
v_{xx}	the speed of the descending feature *xx*

w the dimensionless parameter of nonlinearity
w_0 the pump wave nonlinearity parameter
w_{th} the modulational instability threshold (equation (A3))
Γ_{mi} the modulational instability growth rate (equation (A4))
Γ_c the conversion rate (equation (A10))
Ω the frequency of slow oscillations
α_t^{ion} the relative density of ionizing ($\varepsilon > \varepsilon_{ion}$) electrons
α_t^{dl} the threshold value of α_t^{ion} for DL
$\Delta\theta_b$ a half-power (−3 dB) width of the pump or radar beam
ε_{ion} the ionization energy
ε_{min} (ε_{max}) the minimum (maximum) energy of the accelerated electron distribution
θ_0 incidence angles of the pump wave
θ_s the Spitze angle
λ_r the resonant (Bragg scatter) wavelength
λ_T the mean free path of thermal electrons
μ the electron-to-ion mass ratio
ν_{il} the frequency of inelastic collisions
ν_{ion} the ionization frequency
τ_{st} the growth time of striations
$\widetilde{\omega}_0$ the frequency mismatch between the pump and plasma frequencies
$\widetilde{\omega}_A$ and $\widetilde{\omega}_{mz}$ the frequency mismatch at h_A and h_{mz}, respectively

Acknowledgments
E.M. and T.P. were supported by Air Force Office of Scientific Research. B.E. was supported by the Engineering and Physical Sciences Research Council (EPSRC), UK, grant EP/M009386/1. Support for B.W. was provided by DARPA-DSO under contract HR0011-09-C-0099 and by ONR under grant N00014-03-1-0165. S.G (section 2.2) was supported by Russian Scientific Foundation project 14-12-00706. NL was supported by the European Research Council under the Program FP7/2007-2013)/ERC grant agreement 320839 and the Research Council of Norway under contracts 208028/F50, 216872/F50 and 223252/F50 (CoE). We thank Ranvir Dhillon for providing the EISCAT UHF radar ion line spectra and the reviewers for valuable comments. Experimental and simulation data supporting Figures 6–7 and Figures 9–10 can be requested from B. Watkins (e-mail: ualaska-watkins@usa.net) and E. Mishin (e-mail: evgeny.mishin@us.af.mil), respectively.

References

Ashrafi, M., M. Kosch, K. Kaila, and B. Isham (2007), Spatiotemporal evolution of radio wave pump-induced ionospheric phenomena near the fourth electron gyroharmonic, *J. Geophys. Res.*, *112*, A05314, doi:10.1029/2006JA011938.
Bernhardt, P., C. Tepley, and L. Duncan (1989), Airglow enhancements associated with plasma cavities formed during ionospheric heating experiments, *J. Geophys. Res.*, *94*, 9071–9092.
Bernhardt, P., et al. (2013), Artificial interactions in the high latitude ionosphere, paper presented at RF Ionospheric Interactions Workshop, Arecibo, Puerto Rico.
Bilitza, D., L. McKinnell, B. Reinisch, and T. Fuller-Rowell (2011), The international reference ionosphere (IRI) today and in the future, *J. Geod.*, *85*, 909–920, doi:10.1007/s00190-010-0427-x.
Blagoveshchenskaya, N., T. Borisova, V. Kornienko, B. Thidė, M. Rietveld, M. Kosch, and T. Bösinger (2005), Phenomena in the ionosphere-magnetosphere system induced by injection of powerful HF radio waves into nightside auroral ionosphere, *Ann. Geophys.*, *23*, 87–100.
Borisova, T., N. Blagoveshchenskaya, A. Kalishin, M. Kosch, A. Senior, M. Rietveld, T. Yeoman, and I. Hagström (2014), Phenomena in the high-latitude ionospheric region induced by a HF heater wave at frequencies near the fourth electron gyroharmonic, *Radiophys. Quantum Electron.*, *57*, 1–19.
Bychenkov, V., V. Silin, and S. Uryupin (1988), Ion-acoustic turbulence and anomalous transport, *Phys. Rep.*, *164*, 119–215.
Carlson, H., V. Wickwar, and G. Mantas (1982), Observations of fluxes of suprathermal electrons accelerated by HF excited Langmuir instabilities, *J. Atmos. Terr. Phys.*, *12*, 1089–1100.
Cheung, P., M. Sulzer, D. DuBois, and D. Russell (2001), High-power high-frequency-induced Langmuir turbulence in the smooth ionosphere at Arecibo. II. Low duty cycle, altitude-resolved observations, *Phys. Plasmas*, *8*, 802–812.
Dhillon, R. S., and T. R. Robinson (2005), Observations of time dependence and aspect sensitivity of regions of enhanced UHF backscatter associated with RF heating, *Ann. Geophys.*, *23*, 75–85.
Dimant, Y., A. Gurevich, and K. Zybin (1992), Acceleration of electrons under the action of intense radio-waves near electron cyclotron harmonics, *J. Atmos. Terr. Phys.*, *54*, 425–436.
Djuth, F., P. Stubbe, M. Sulzer, H. Kohl, M. Rietveld, and J. Elder (1994), Altitude characteristics of plasma turbulence excited with the Tromsø superheater, *J. Geophys. Res.*, *99*, 333–339.
Djuth, F., T. Pedersen, E. Gerken, P. Bernhardt, C. Selcher, W. Bristow, and M. Kosch (2005), Ionospheric modification at twice the electron cyclotron frequency, *Phys. Rev. Lett.*, *94*, 125001, doi:10.1103/PhysRevLett.94.125001.
DuBois, D. F., A. H. H. A. Rose, and D. Russell (1993), Space and time distribution of HF excited Langmuir turbulence in the ionosphere: Comparison of theory and experiment, *J. Geophys. Res.*, *98*, 17,543–17,567.
Eliasson, B. (2008), Full-scale simulation study of the generation of topside ionospheric turbulence using a generalized Zakharov model, *Geophys. Res. Lett.*, *35*, L11104, doi:10.1029/2008GL033866.
Eliasson, B. (2013), Full-scale simulations of ionospheric Langmuir turbulence, *Mod. Phys. Lett. B*, *27*(8), 1330005, doi:10.1142/S0217984913300056.
Eliasson, B., and K. Papadopoulos (2015), Numerical study of anomalous absorption of O mode waves on magnetic field-aligned striations, *Geophys. Res. Lett.*, *42*, 2603–2611, doi:10.1002/2015GL063751.
Eliasson, B., X. Shao, G. Milikh, E. V. Mishin, and K. Papadopoulos (2012), Numerical modeling of artificial ionospheric layers driven by high-power HF-heating, *J. Geophys. Res.*, *117*, A10321, doi:10.1029/2012JA018105.
Eliasson, B., G. Milikh, X. Shao, E. Mishin, and K. Papadopoulos (2015), Incidence angle dependence of Langmuir turbulence and artificial ionospheric layers driven by high-power HF-heating, *J. Plasma Phys.*, *81*, 415810201, doi:10.1017/S0022377814000968.
Fejer, J. (1979), Ionospheric modification and parametric instabilities, *Rev. Geophys.*, *17*, 135–153, doi:10.1029/2012JA018105.
Forslund, D. (1970), Instabilities associated with heat conduction in the solar wind and their consequences, *J. Geophys. Res.*, *75*, 17–28, doi:10.1029/JA075i001p00017.

Galeev, A., R. Sagdeev, V. Shapiro, and V. Shevchenko (1977), Langmuir turbulence and dissipation of high-frequency energy, *Sov. Phys. JETP*, *46*, 711–719.

Galeev, A., R. Sagdeev, V. Shapiro, and V. Shevehenko (1983), Beam plasma discharge and suprathermal electron tails, in *Active Experiments in Space (Symposium at Alpbach, Austria), ESA SP-195*, Paris, Eur. Space Agency Spec. Publ., pp. 151–155.

Galinsky, V., V. Shevchenko, E. Mishin, and M. Starks (2011), Numerical modeling of 3D weak turbulence driven by high-power VLF pump waves in the topside ionosphere, *Geophys. Res. Lett.*, *38*, L16105, doi:10.1029/2011GL048441.

Gelinas, L., M. Kelley, M. Sulzer, E. Mishin, and M. Starks (2003), In situ observations during an HF heating experiment at Arecibo: Evidence for Z-mode and electron cyclotron harmonic effects, *J. Geophys. Res.*, *108*(A10), 1382, doi:10.1029/2003JA009922.

Grach, S. (1979), Thermal parametric instability in ionospheric plasma at frequencies close to ω_{He} and $2\omega_{He}$, *Radiophys. Quantum Electron.*, *22*, 357–361.

Grach, S., N. Mityakov, V. Rapoport, and V. Trakhtengertz (1981), Thermal parametric turbulence in a plasma, *Physica D*, *2*, 102–106.

Grach, S., S. Sergeev, V. Yashnov, and V. Kotov (2008), Spectra of stimulated electromagnetic emission of the ionosphere during pump frequency sweeping near gyroharmonics. II. Discussion of the results, *Radiophys. Quantum Electron.*, *51*, 499–514.

Grach, S., E. Sergeev, E. Mishin, A. Shindin, and M. McCarrick (2015), Intermediate downshifted maximum of stimulated electromagnetic emission at high-power HF heating: A new twist on an old problem, *J. Geophys. Res. Space Physics*, *120*, 666–674, doi:10.1002/2014JA020423.

Gurevich, A. (2007), Nonlinear effects in the ionosphere, *Phys. Usp.*, *50*, 1091–1121, doi:10.1070/PU2007v050n11ABEH006212.

Gurevich, A., A. Lukyanov, and K. Zybin (1996), Anomalous absorption of powerful radio waves on the striations developed during ionospheric modification, *Phys. Lett. A*, *211*, 363–372.

Gurevich, A., K. Zybin, H. Carlson, and T. Pedersen (2002), Magnetic zenith effect in ionospheric modifications, *Phys. Lett. A*, *305*, 264–274.

Gustavsson, B., B. Brändström, A. Steen, T. Sergienko, T. Leyser, M. Rietveld, T. Aso, and M. Erjii (2002), Nearly simultaneous images of HF-pump enhanced airglow at 6300 Å and 5577 Å, *Geophys. Res. Lett.*, *29*(24), 2220, doi:10.1029/2002GL015350.

Gustavsson, B., T. Leyser, M. Kosch, M. Rietveld, Å. Steen, B. Brändström, and T. Aso (2006), Electron gyroharmonic effects in ionization and electron acceleration during high-frequency pumping in the ionosphere, *Phys. Rev. Lett.*, *97*, 195002, doi:10.1103/PhysRevLett.97.195002.

Gustavsson, B., M. Rietveld, N. Ivchenko, and M. Kosch (2010), Rise and fall of electron temperatures: Ohmic heating of ionospheric electrons from underdense HF radio wave pumping, *J. Geophys. Res.*, *115*, A12332, doi:10.1029/2010JA015873.

Guzdar, P., P. Chaturvedi, K. Papadopoulos, and S. Ossakow (1998), The thermal self-focussing instability near the critical surface in the high-latitude ionosphere, *J. Geophys. Res.*, *103*, 2231–2237.

Huang, J., and S. Kuo (1994), A theoretical model for the broad upshifted maximum in the stimulated electromagnetic emission spectrum, *J. Geophys. Res.*, *99*, 19,569–19,576.

Huang, J., and S. P. Kuo (1995), A generation mechanism for the downshifted peak in stimulated electromagnetic emission spectrum, *J. Geophys. Res.*, *100*, 21,433–21,438, doi:10.1029/95JA02302.

Hussein, A., W. Scales, and J. Huang (1998), Theoretical and simulation studies of broad up-shifted sideband generation in ionospheric stimulated radiation, *Geophys. Res. Lett.*, *25*, 955–958.

Hysell, D., and E. Nossa (2009), Artificial E-region field-aligned plasma irregularities generated at pump frequencies near the second electron gyroharmonic, *Ann. Geophys.*, *27*, 2711–2720.

Hysell, D., R. Miceli, E. Kendall, N. Schlatter, R. Varney, B. Watkins, T. Pedersen, P. Bernhardt, and J. Huba (2014), Heater-induced ionization inferred from spectrometric airglow measurements, *J. Geophys. Res. Space Physics*, *119*, 2038–2045, doi:10.1002/2013JA019663.

Isham, B., T. Hagfors, E. Mishin, M. Rietveld, C. LaHoz, W. Kofman, and T. Leyser (1999), A search for the location of the HF excitation of enhanced ion acoustic and Langmuir waves with EISCAT and the Tromsø heater, *Radiophys. Quantum Electron.*, *42*, 607–618.

Istomin, Y., and T. Leyser (1995), Parametric decay of an electromagnetic wave near electron cyclotron harmonics, *Phys. Plasmas*, *2*, 2084–2097.

Kadomtsev, B. (1965), *Plasma Turbulence*, Academic, San Diego, Calif.

Kosch, M., T. Rietveld, T. Hagfors, and T. Leyser (2000), High-latitude HF-induced airglow displaced equatorwards of the pump beam, *Geophys. Res. Lett.*, *27*, 2817–2820, doi:10.1029/2000GL003754.

Kosch, M., M. Rietveld, A. Senior, I. McCrea, A. Kavanagh, B. Isham, and F. Honary (2004), Novel artificial optical annular structures in the high latitude ionosphere, *Geophys. Res. Lett.*, *31*, L12805, doi:10.1029/2004GL019713.

Kosch, M., T. Pedersen, J. Hughes, R. Marshall, E. Gerken, A. Senior, D. Sentman, M. McCarrick, and F. Djuth (2005), Artificial optical emissions at HAARP for pump frequencies near the third and second gyroharmonic, *Ann. Geophys.*, *23*, 1585–1592.

Kosch, M., T. Pedersen, E. Mishin, S. Oyama, J. Hughes, A. Senior, B. Watkins, and B. Bristow (2007a), Coordinated optical and radar observations of ionospheric pumping for a frequency pass through the second electron gyroharmonic at HAARP, *J. Geophys. Res.*, *112*, A06325, doi:10.1029/2006JA012146.

Kosch, M., T. Pedersen, E. Mishin, M. Starks, E. Gerken-Kendall, D. Sentman, S. Oyama, and B. Watkins (2007b), Temporal evolution of pump beam self-focusing at the high-frequency active auroral research program, *J. Geophys. Res.*, *112*, A08304, doi:10.1029/2007JA012264.

Kosch, M., Y. Ogawa, M. Rietveld, S. Nozawa, and R. Fujii (2010), An analysis of pump-induced artificial ionospheric ion upwelling at EISCAT, *J. Geophys. Res.*, *115*, A12317, doi:10.1029/2010JA015854.

Kuo, S. (2003), Parametric excitation of lower hybrid waves by electron plasma waves, *Phys. Lett. A*, *307*, 244–248.

Kuo, S. (2015), Ionospheric modifications in high frequency heating experiments, *Phys. Plasmas*, *22*, 012901, doi:10.1063/1.4905519.

Kuo, S., M. Lee, and P. Kossey (1997), Excitation of oscillating two-stream instability by upper hybrid pump in ionospheric heating experiments at Tromsø, *Geophys. Res. Lett.*, *24*, 2969–2972.

Lehtinen, N., and U. Inan (2008), Radiation of ELF/VLF waves by harmonically varying currents into a stratified ionosphere with application to radiation by a modulated electrojet, *J. Geophys. Res.*, *113*, A06301, doi:10.1029/2007JA012911.

Leyser, T. B. (2001), Stimulated electromagnetic emissions by high-frequency electromagnetic pumping of the ionospheric plasma, *Space Sci. Rev.*, *98*, 223–328, doi:10.1023/A:1013875603938.

Macmillan, S., et al. (2003), The 9th-generation international geomagnetic reference field, *Geophys. J. Int.*, *155*, 1051–1056, doi:10.1111/j.1365-246X.2003.02102.x.

Mahmoudian, A., W. Scales, P. Bernhardt, A. Samimi, E. Kendall, J. Ruohoniemi, B. Isham, O. Vega-Cancel, and M. Bordikar (2013), Ion gyro-harmonic structuring in the stimulated radiation spectrum and optical emissions during electron gyro-harmonic heating, *J. Geophys. Res. Space Physics*, *118*, 1270–1287, doi:10.1002/jgra.50167.

Majeed, T., and D. J. Strickland (1997), New survey of electron impact cross sections for photoelectron and auroral electron energy loss calculations, *J. Phys. Chem. Ref. Data*, *26*, 335–349.

Milikh, G., E. Mishin, I. Galkin, A. Vartanyan, C. Roth, and B. Reinisch (2010), Ion outflows and artificial ducts in the topside ionosphere at HAARP, *Geophys. Res. Lett.*, *37*, L18102, doi:10.1029/2010GL044636.
Mishin, E. (1974), Heat transport in the solar wind, *Astrophys. Space Sci.*, *27*, 367–382.
Mishin, E., and V. Fiala (1995), Radiation of whistlers by the ion-acoustic turbulence in the ionosphere, *J.Geophys. Res.*, *100*, 19,695–19,700.
Mishin, E., and T. Pedersen (2011), Ionizing wave via high-power HF acceleration, *Geophys. Res. Lett.*, *38*, L01105, doi:10.1029/2010GL046045.
Mishin, E., and K. Schlegel (1994), On incoherent-scatter plasma lines in aurora, *J. Geophys. Res.*, *99*, 11,391–11,399.
Mishin, E., and V. Telegin (1986), Spectrum of suprathermal electrons in the auroral plasma, *Sov. J. Plasma Phys.*, *12*, 509–511.
Mishin, E., H. Carlson, and T. Hagfors (2000), On the electron distribution function in the *F* region and airglow enhancements during HF modification experiments, *Geophys. Res. Lett.*, *27*, 2857–2860.
Mishin, E., T. Hagfors, and B. Isham (2001), A generation mechanism for topside enhanced incoherent backscatter during high frequency modification experiments in Tromsø, *Geophys. Res. Lett.*, *28*, 479–482.
Mishin, E., W. Burke, and T. Pedersen (2004), On the onset of HF-induced airglow at magnetic zenith, *J. Geophys. Res.*, *109*, A02305, doi:10.1029/2003JA010205.
Mishin, E., M. Kosch, T. Pedersen, and W. Burke (2005a), HF-induced airglow at magnetic zenith: Coexistence of the thermal and parametric instabilities near electron gyroharmonics, *Geophys. Res. Lett.*, *32*, L23106, doi:10.1029/2005GL023864.
Mishin, E., W. Burke, and T. Pedersen (2005b), HF-induced airglow at magnetic zenith: Theoretical considerations, *Ann. Geophys.*, *23*, 47–53.
Mjølhus, E. (1990), On linear conversion in a magnetized plasma, *Radio Sci.*, *25*, 1321–1339.
Mjølhus, E. (1993), On the small scale striation effect in ionospheric radio modification experiments near harmonics of the electron gyro frequency, *J. Atmos. Terr. Phys.*, *55*, 907–918.
Mjølhus, E., E. Helmersen, and D. DuBois (2003), Geometric aspects of HF driven Langmuir turbulence in the ionosphere, *Nonlinear Processes Geophys.*, *10*, 151–177.
Musher, S. L., A. M. Rubenchik, and B. I. Sturman (1978), Collective effects associated with lower hybrid heating of plasma, *Plasma Phys.*, *20*, 1131–1150.
Mutiso, C., J. Hughes, G. Sivjee, T. Pedersen, B. Gustavsson, and M. Kosch (2008), Previously unreported optical emissions generated during ionospheric heating, *Geophys. Res. Lett.*, *35*, L14103, doi:10.1029/2008GL034563.
Oyama, S., B. Watkins, F. Djuth, M. Kosch, P. Bernhardt, and C. Heinselman (2006), Persistent enhancement of the HF pump-induced plasma line measured with a UHF diagnostic radar at HAARP, *J. Geophys. Res.*, *111*, A06309, doi:10.1029/2005JA011363.
Oyama, S., and B. Watkins (2007), Aspect angle dependency of the HF modification measured with MUIR at HAARP, *Eos Trans. AGU*, *88*(52), Fall Meet. Suppl., Abstract SA11A–0294.
Pedersen, T., M. McCarrick, E. Gerken, C. Selcher, D. Sentman, H. Carlson, and A. Gurevich (2003), Magnetic zenith enhancement of HF radio-induced airglow production at HAARP, *Geophys. Res. Lett.*, *30*(4), 1169–1172, doi:10.1029/2002GL016096.
Pedersen, T., B. Gustavsson, E. Mishin, E. MacKenzie, H. C. Carlson, M. Starks, and T. Mills (2009), Optical ring formation and ionization production in high-power HF heating experiments at HAARP, *Geophys. Res. Lett.*, *36*, L18107, doi:10.1029/2009GL040047.
Pedersen, T., B. Gustavsson, E. Mishin, E. Kendall, T. Mills, H. C. Carlson, and A. L. Snyder (2010), Creation of artificial ionospheric layers using high-power HF waves, *Geophys. Res. Lett.*, *37*, L02106, doi:10.1029/2009GL041895.
Pedersen, T., M. McCarrick, B. Reinisch, B. Watkins, R. Hamel, V. Paznukhov (2011), Production of artificial ionospheric layers by frequency sweeping near the 2nd gyroharmonic, *Ann. Geophys.*, *29*, 47–47, doi:10.5194/angeo-29-47-2011.
Rietveld, M., M. Kosch, N. Blagoveshchenskaya, V. Kornienko, T. Leyser, and T. Yeoman (2003), Ionospheric electron heating, optical emissions and striations induced by powerful HF radio waves at high latitudes: Aspect angle dependence, *J. Geophys. Res.*, *108*(A4), 1141, doi:10.1029/2002JA009543.
Robinson, T. (1989), The heating of the high latitude ionosphere by high-power radio waves, *Phys. Rep.*, *179*, 79–209.
Robinson, P. (1997), Nonlinear wave collapse and strong turbulence, *Rev. Mod. Phys.*, *69*, 507–573.
Rosenbluth, M., and N. Rostoker (1962), Scattering of electromagnetic waves by a nonequilibrium plasma, *Phys. Fluids*, *5*, 776–788.
Sagdeev, R. (1979), The 1976 Oppenheimer lectures: Critical problems in plasma astrophysics, *Rev. Mod. Phys.*, *51*, 1–20.
Samimi, A., W. A. Scales, P. A. Bernhardt, S. J. Briczinski, and M. J. McCarrick (2013), Ion gyroharmonic structures in stimulated radiation during second electron gyroharmonic heating: 1. Theory, *J. Geophys. Res. Space Physics*, *118*, 502–514, doi:10.1029/2012JA018146.
Samimi, A., W. A. Scales, P. A. Bernhardt, S. J. Briczinski, and M. J. McCarrick (2014), Ion gyroharmonic structures in stimulated radiation during second electron gyroharmonic heating: 2. Simulations, *J. Geophys. Res. Space Physics*, *119*, 462–478, doi:10.1002/2013JA019341.
Senior, A., N. D. Borisov, M. J. Kosch, T. K. Yeoman, F. Honary, and M. T. Rietveld (2004), Multi-frequency HF radar measurements of artificial F-region field-aligned irregularities, *Ann. Geophys.*, *22*, 3503–3511.
Sergeev, E., S. Grach, A. Shindin, E. Mishin, P. Bernhardt, S. Briczinski, B. Isham, M. Broughton, J. LaBelle, and B. Watkins (2013), Artificial ionospheric layers during pump frequency stepping near the 4th gyroharmonic at HAARP, *Phys. Rev. Lett.*, *110*, 065002.
Shapiro, V., and V. Shevchenko (1984), Strong turbulence of plasma oscillations, in *Basic Plasma Physics*, vol. 2, edited by A. Galeev and R. Sudan, pp. 123–182, New York, North-Holland.
Starodubtsev, M., V. Nazarov, and A. Kostrov (2007), Laboratory study of nonlinear trapping of magnetized Langmuir waves inside a density depletion, *Phys. Rev. Lett.*, *98*, 195001, doi:10.1103/PhysRevLett.98.195001.
Stubbe, P., H. Kohl, and M. T. Rietveld (1992), Langmuir turbulence and ionospheric modification, *J. Geophys. Res.*, *97*, 6285–6297.
Stubbe, P., A. J. Stocker, F. Honary, T. R. Robinson, and T. B. Jones (1994), Stimulated electromagnetic emissions (SEE) and anomalous HF wave absorption near electron gyroharmonics, *J. Geophys. Res.*, *99*, 6233–6246.
Stubbe, P., H. Kopka, B. Thidé, and H. Derblom (1984), Stimulated electromagnetic emission: A new technique to study the parametric decay instability in the ionosphere, *J. Geophys. Res.*, *89*, 7523–7536.
Stubbe, P. (1996), Review of ionospheric modification experiments at Tromsø, *J. Atmos. Terr. Phys.*, *58*, 349–368.
Thidé, B., H. Kopka, and P. Stubbe (1982), Observations of stimulated scattering of a strong high frequency radio wave in the ionosphere, *Phys. Rev. Lett.*, *49*, 1561–1564, doi:10.1103/PhysRevLett.49.1561.
Thidé, B., E. N. Sergeev, S. M. Grach, T. B. Leyser, and T. D. Carozzi (2005), Competition between Langmuir and upper-hybrid turbulence in a high-frequency-pumped ionosphere, *Phys. Rev. Lett.*, *95*, 255002, doi:10.1103/PhysRevLett.95.255002.
Vaskov, V., and A. Gurevich (1977), Resonance instability of small-scale plasma perturbations, *Sov. Phys. JETP*, *46*, 487–494.
Volokitin, A., and E. Mishin (1979), Relaxation of an electron beam in a plasma with infrequent collisions, *Sov. J. Plasma Phys*, *5*, 654–656.
Volokitin, A., and E. Mishin (1995), Theory of incoherent scattering in a weakly turbulent ionospheric plasma, *Radiophys. Quantum Electron.*, *38*, 359–363, doi:10.1007/BF01037768.
Vuthaluru, R., R. A. Vincent, D. A. Holdsworth, and I. M. Reid (2002), Collision frequencies in the D-region, *J. Atmos. Sol. Terr. Phys.*, *64*, 2043–2054, doi:10.1016/S1364-6826(02)00220-1.

Wang, J., D. Newman, and M. Goldman (1997), Vlasov simulations of electron heating by Langmuir turbulence near the critical altitude in the radiation-modified ionosphere, *J. Atmos. Sol. Terr. Phys.*, *59*, 2461–2474, doi:10.1016/S1364-6826(96)00140-X.

Zakharov, V. (1984), Collapse and self-focusing of Langmuir waves, in *Basic Plasma Physics*, vol. 2, edited by A. Galeev and R. Sudan, pp. 81–121, North-Holland, New York.

Zhou, H. L., J. Huang, and S. P. Kuo (1994), Cascading of the upper hybrid/electron Bernstein wave in ionospheric heating experiments, *Phys. Plasmas*, *1*, 3044–3052.